



Superharmonic resonance of the quasi-zero-stiffness vibration isolator and its effect on the isolation performance

Chaoran Liu · Kaiping Yu

Received: 18 March 2019 / Accepted: 27 January 2020 / Published online: 11 February 2020
© Springer Nature B.V. 2020

Abstract Quasi-zero-stiffness (QZS) vibration isolator seeks better isolation performance by lowering the natural frequency while maintaining the same static load bearing capacity as equivalent linear isolator. In previous works on QZS isolator, the steady-state response is usually assumed to be a single harmonic at the excitation frequency. However, the QZS isolator can actually exhibit various nonlinear dynamic behaviors such as multi-period responses and chaos. Even the simplest period-1 response, which occurs under most parameter conditions, is not a single harmonic, but contains superharmonics. This paper focuses on the superharmonic resonance that exists in the period-1 response. Both numerical simulation and analytical analysis are conducted; it is shown that there exist multiple superharmonics in the response, the frequencies of which are odd times the excitation frequency, but they are not very apparent when the excitation frequency is higher than a certain value. To characterize the overall properties of these superharmonics, two indices are proposed and analyzed in this paper. In addition, effect of superharmonic resonance on the vibration isolation performance is investigated based on the redefined transmissibility.

C. Liu · K. Yu ()
Department of Astronautic Science and Mechanics, Harbin Institute of Technology, No. 92 West Dazhi Street, Harbin 150001, China

K. Yu
e-mail: kaipingyu1968@gmail.com
C. Liu
e-mail: chaoranhit@gmail.com

Keywords Quasi-zero stiffness · Nonlinear vibration · Superharmonic resonance · Superharmonic energy factor · Superharmonic truncation frequency

1 Introduction

Vibrations in engineering often bring undesirable consequences, such as wear of mechanical components, noise generation and passenger comfort reduction. Therefore, vibration isolation has gradually become a key requirement for many engineering systems, especially high-precision equipment. Traditional linear passive vibration isolation approaches have to confront a trade-off: A lower stiffness is needed to reduce the natural frequency and thus widen the frequency range of isolation, but this may cause an excessive static displacement [1].

In fact, an ideal passive vibration isolator is supposed to possess both low dynamic stiffness to reduce the natural frequency and high static stiffness to reduce the static displacement, which requires to introduce stiffness nonlinearity [2]. The dynamic stiffness means the derivative of the restoring force with respect to the displacement, while the static stiffness means the ratio of the restoring force at the static equilibrium position to the static displacement [3,4]. The concept of *high-static–low-dynamic-stiffness* (HSLDS) vibration isolator is a passive vibration isolation approach proposed in recent decades to overcome the disadvantages of linear isolator, which is usually developed by connecting

a negative stiffness mechanism in parallel with a conventional linear spring element with positive stiffness. The negative stiffness mechanism is used to lower the total dynamic stiffness of the isolator, while the positive stiffness element is used to withstand the isolated object and to ensure the total dynamic stiffness is non-negative. Most of the HSLDS isolators have symmetric stiffness characteristics with respect to the static equilibrium point, and the minimum dynamic stiffness of the HSLDS isolator can be designed to zero by well-chosen system parameters, to achieve the lowest natural frequency. If the dynamic stiffness of the negative stiffness mechanism at the static equilibrium position exactly counterparts the stiffness of the linear spring element, the minimum dynamic stiffness of the HSLDS isolator becomes zero, and then, it is called the *quasi-zero-stiffness* (QZS) vibration isolator [5].

QZS isolators are numerous in the literature, among which the most thoroughly studied is the one composed of three springs [6–10], two of which are oblique acting as negative stiffness mechanism, and another is vertical to provide positive stiffness. Lan et al. [11] have carried out an experiment on this kind of QZS isolator using planar springs. Another kind of material that can be exploited to construct QZS vibration isolators is the beam with large deformation, such as Euler buckled beam [12–14], slightly curved beam [15] and sliding beam [16], since they have beneficial nonlinear characteristics and therefore can be employed to obtain negative stiffness by well-designed configurations. In recent years, the utilization of magnets or magnetic springs to build QZS vibration isolators has gained more and more attention, because the application of magnetic forces does not require direct contact, and thus, magnetic QZS isolators are easier to manufacture and implement. References [17–22] have described some QZS vibration isolators based upon magnetic springs, the differences among which lie in the arrangement and the shape of magnets. There are also researchers devoted to some other issues concerned with QZS isolators, such as the optimization design of QZS isolators [23, 24], the torsion QZS isolators [21, 25] and the two-stage QZS vibration isolation systems [26, 27], in order to further facilitate and broaden the application of the QZS vibration isolation strategy.

In the previous studies on QZS vibration isolators, there is a basic assumption that the steady-state response takes the form of single harmonic at the excitation frequency. This assumption is beneficial for sim-

plifying the analytical calculation and may be legitimate in some practical cases. However, as a nonlinear dynamical system, the QZS isolator can actually exhibit many complex dynamic behaviors, such as multi-period responses, bifurcations and chaos. Even the simplest period-1 response is not a single harmonic, but contains multiple superharmonics, which are more apparent under low-frequency excitation. Although the superharmonic components are relatively small compared to the primary resonance, the assumption of single-harmonic response may not be able to describe the dynamic response characteristics of the QZS isolator properly. Besides, the vibration isolation performance, which is related to the dynamic response, cannot be evaluated accurately if the superharmonic components are ignored.

The main focus of this paper is placed on the superharmonic resonance of the QZS vibration isolator that exists in the period-1 response and its effect on the vibration isolation performance. A QZS isolator composed of springs and rods is taken as the research object. Numerical simulations are performed first to validate the existence of the superharmonic resonance and preliminarily obtain its characteristics. The harmonic balance method (HBM) is employed to find the analytical superharmonic response solution; the stability is analyzed using a semi-analytical method. Two indices characterizing the overall properties of the superharmonic components are proposed, which are *superharmonic energy factor* and *superharmonic truncation frequency*. Considering that the previously defined transmissibility is no longer applicable when multiple harmonics exist in the response, the transmissibility is redefined in this paper to quantify the vibration isolation performance and investigate the effect of superharmonic resonance on the isolation performance.

This paper is organized as follows: In Sect. 2, we conduct the static analysis of the QZS isolator and then formulate the equation of motion. Section 3 presents the bifurcation scenarios and various dynamic behaviors of the QZS isolator and, most importantly, validates the existence of the superharmonic resonance. In Sect. 4, the superharmonic resonance of the QZS isolator is analytically studied in detail. In Sect. 5, effect of the superharmonic resonance on the vibration isolation performance is investigated. The conclusions are drawn in Sect. 6.

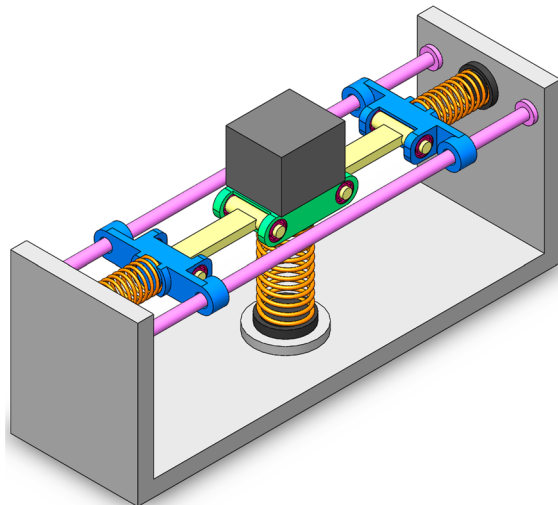


Fig. 1 QZS vibration isolator being studied

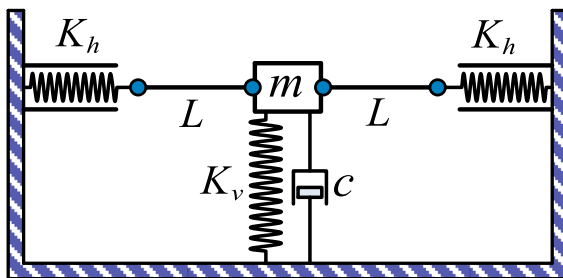


Fig. 2 Simplified mechanical model of the QZS vibration isolator

2 Mathematical modeling of the QZS isolator

This paper takes the QZS vibration isolator shown in Fig. 1 as research object, which is composed of a vertical spring, two pre-compressed horizontal springs with the same stiffness two sliding blocks and two connecting rods with the same length. The vertical spring provides positive stiffness; the combination of horizontal springs, sliding blocks and rods provides negative stiffness and thus can be called the *negative stiffness mechanism* (NSM). The position in Fig. 1 is just the static equilibrium position where the rods become horizontal and the horizontal springs are compressed to the maximum. Figure 2 depicts the simplified mechanical model of the HSLDS-AS isolator, in which the isolated object is represented by the lumped mass m , and all components are considered massless except the isolated object.

It is instructive to examine first the static characteristics of the negative stiffness mechanism. When the isolated object experiences a vertical displacement X from the initial static equilibrium position, the compression of each horizontal spring becomes

$$\delta = \sqrt{L^2 - X^2} + \delta_0 - L \quad (1)$$

where δ_0 is the initial pre-compression at the static equilibrium position and L is the length of the rod. The force exerted by each of the horizontal springs is therefore

$$F_{\text{hor}} = K_h \delta = K_h (\sqrt{L^2 - X^2} + \delta_0 - L) \quad (2)$$

The restoring force of the negative stiffness mechanism is calculated by

$$F_{\text{nsm}} = -2F_{\text{hor}} \tan \theta \quad (3)$$

where θ is the angle between the axis of a rod and the horizontal line, whose tangent value is given by

$$\tan \theta = \frac{X}{\sqrt{L^2 - X^2}} \quad (4)$$

Substituting Eqs. (2) and (4) into Eq. (3) gives the force–displacement relationship of the NSM:

$$F_{\text{nsm}}(X) = 2K_h \left(\frac{L - \delta_0}{\sqrt{L^2 - X^2}} - 1 \right) X \quad (5)$$

By introducing $f_{\text{nsm}} = F_{\text{nsm}}/(K_v L)$, $\lambda = K_h/K_v$, $\alpha = \delta_0/L$ and $x = X/L$ ($|x| < 1$), this relationship can be written in the non-dimensional form

$$f_{\text{nsm}}(x) = 2\lambda \left(\frac{1 - \alpha}{\sqrt{1 - x^2}} - 1 \right) x \quad (6)$$

Figure 3 shows the force–displacement relationship of the NSM under different values of pre-compression ratio α . It can be seen that a larger pre-compression ratio is beneficial for obtaining a more negative stiffness around the static equilibrium position where $x = 0$ and a wider displacement range that ensures negative stiffness.

Differentiating Eq. (6) with respect to the non-dimensional displacement x results in the

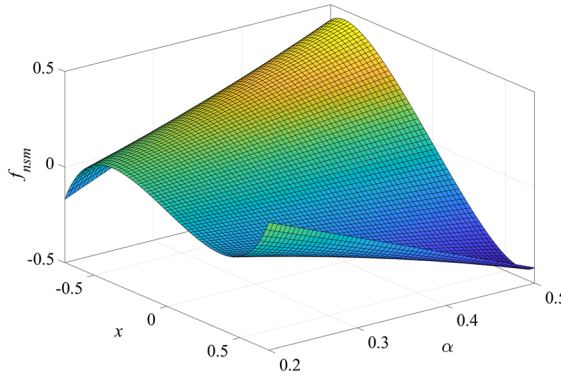


Fig. 3 Force–displacement relationship of the NSM under different values of α ($\lambda = 1$)

non-dimensional stiffness–displacement relationship of the NSM:

$$k_{\text{nsm}}(x) = 2\lambda \left[\frac{1-\alpha}{(1-x^2)^{\frac{3}{2}}} - 1 \right] \quad (7)$$

The stiffness is a minimum at the static equilibrium position, which is given by

$$k_{\text{nsm}(\min)} = k_{\text{nsm}}(0) = -2\lambda\alpha \quad (8)$$

The displacement range that ensures negative stiffness (i.e., $k_{\text{nsm}}(x) < 0$) is

$$|x| < \sqrt{1 - (1 - \alpha)^{\frac{2}{3}}} \quad (9)$$

The whole isolator is a parallel combination of the negative stiffness mechanism discussed above and a vertical spring. Therefore, the restoring force–displacement relationship of the whole isolator is obtained by adding the force–displacement relationships of the negative stiffness mechanism and the vertical spring together:

$$\begin{aligned} F_{\text{res}}(X) &= F_{\text{nsm}}(X) + K_v X \\ &= 2K_h \left(\frac{L - \delta_0}{\sqrt{L^2 - X^2}} - 1 \right) X + K_v X \end{aligned} \quad (10)$$

where the constant term (which is caused by the pre-compression of the vertical spring to withstand the weight of the isolated object) is omitted, and K_v is the stiffness of the vertical spring. Using a similar way of non-dimensionalization, the force–displacement rela-

tionship can be written in non-dimensional form as

$$f_{\text{res}}(x) = 2\lambda \left(\frac{1-\alpha}{\sqrt{1-x^2}} - 1 \right) x + x \quad (11)$$

where $f_{\text{res}} = F_{\text{res}}/(K_v L)$. Differentiating Eq. (11) with respect to the non-dimensional displacement x gives the non-dimensional stiffness–displacement relationship of the isolator:

$$k(x) = 2\lambda \left[\frac{1-\alpha}{(1-x^2)^{\frac{3}{2}}} - 1 \right] + 1 \quad (12)$$

The minimum stiffness is $k(0) = 1 - 2\lambda\alpha$. In order to realize quasi-zero stiffness and thus become a QZS isolator, we need to set the stiffness at static equilibrium point $k(0)$ to zero, which leads to the relationship between λ and α that gives rise to QZS feature:

$$\lambda\alpha = \frac{1}{2} \quad (13)$$

In the subsequent analysis, Eq. (13) is always held to ensure the QZS feature, and for conciseness, the value of α , which is dependent on the value of λ , is not shown hereafter. Then the (non-dimensional) force–displacement relationship of the isolator with QZS is

$$f_{\text{QZS}} = (2\lambda - 1) \left(\frac{1}{\sqrt{1-x^2}} - 1 \right) x \quad (14)$$

The force–displacement relationship of the QZS isolator under different values of stiffness ratio λ is shown Fig. 4. It can be seen that under the QZS condition, a larger stiffness ratio results in larger degree of nonlinearity.

There are two categories of vibration isolation problems [28]: (a) The force excitation is applied on the isolated object, and the goal is to minimize the force transmitted to the base on which the mass is mounted and (b) the source of vibration is the base, in which case the purpose of vibration isolation is to minimize the vibration of the isolated object. The former case is referred to as the force transmission problem, while the latter as the motion transmission problem.

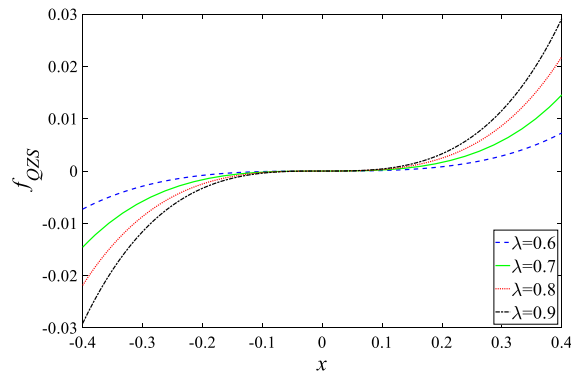


Fig. 4 Force–displacement relationship of the QZS isolator under different values of λ

For the force transmission problem, the equation of motion is

$$m\ddot{X} + c\dot{X} + F_{QZS}(X) = F_0 \cos(\omega t) \quad (15)$$

where $F_0 \cos(\omega t)$ is the excitation force with amplitude F_0 and frequency ω , m is the mass of the isolated object and c is the linear viscous damping coefficient introduced to account for energy dissipation. To non-dimensionalize Eq. (15), the following non-dimensional constants and variables are introduced:

$$\begin{aligned} \omega_n &= \sqrt{\frac{K_v}{m}}; \quad \zeta = \frac{c}{2\sqrt{mK_v}}; \quad f_0 = \frac{F_0}{K_v L}; \quad \mu = \frac{\omega}{\omega_n}; \\ \tau &= \omega_n t \end{aligned} \quad (16)$$

where ω_n is the undamped natural frequency of the equivalent linear isolator with stiffness K_v , ζ is the damping ratio, f_0 is the non-dimensional excitation amplitude, μ is the non-dimensional excitation frequency and τ is the non-dimensional time. Then the non-dimensional equation of motion under force excitation is found to be

$$x'' + 2\zeta x' + (2\lambda - 1) \left(\frac{1}{\sqrt{1-x^2}} - 1 \right) x = f_0 \cos(\mu\tau) \quad (17)$$

where $(\bullet)''$ and $(\bullet)'$ denote differentiation with respect to the non-dimensional time τ . It would considerably simplify subsequent dynamic analysis if the nonlinear component of the dynamic equation Eq. (17) could be described by a polynomial. This can be done by employing the Taylor series expansion, and it is natural

to set the center of expansion at the static equilibrium point; besides, previous studies have shown that satisfactory accuracy can be fulfilled when truncating the approximate polynomial to third order. Therefore, by using the third-order Taylor series approximation, the (non-dimensional) equation of motion can be rewritten as

$$x'' + 2\zeta x' + \beta x^3 = f_0 \cos(\mu\tau) \quad (18)$$

where $\beta = \lambda/ - 12$ can directly reflect the degree of nonlinearity.

For the base transmission problem, the equation of motion is

$$m\ddot{X} + c(\dot{X} - \dot{B}) + F_{QZS}(X - B) = 0 \quad (19)$$

where $B(t) = B_0 \cos(\omega t)$ is the motion of the base. This equation would be considerably simplified if it is transformed into an equation with respect to relative displacement $Y(t) = X(t) - B(t)$. Then by introducing the non-dimensional relative displacement $y = Y/L_0$ and non-dimensional base excitation amplitude $b_0 = B_0/L_0$, the non-dimensional equation of motion with respect to y is obtained as

$$\begin{aligned} y'' + 2\zeta y' + (2\lambda - 1) \left(\frac{1}{\sqrt{1-y^2}} - 1 \right) y \\ = \mu^2 b_0 \cos(\mu\tau) \end{aligned} \quad (20)$$

It can be seen that Eqs. (17) and (20) are essentially the same when only considering the response at a given excitation frequency, whereas they are a little different when considering the frequency response characteristics in the whole frequency range. This paper is concerned with the QZS isolator subjected to harmonic force excitation.

3 Existence of the superharmonic resonance

In this section, we conduct direct numerical integration of the equation of motion Eq. (18) using the fourth-order Runge–Kutta algorithm to observe the possible dynamic behaviors of the QZS isolator under harmonic force excitation and to validate the existence of the superharmonic response and preliminarily obtain its

characteristics. The time step is 1/400 of the harmonically forcing period to guarantee the computational accuracy.

3.1 Preliminary numerical simulations

In this subsection, we vary the values of damping ratio and excitation amplitude in a wide range ($\zeta \in (0, 0.15]$, $f_0 \in (0, 0.4]$) to observe the bifurcation scenarios and the possible response types.

Figure 5a shows the bifurcation diagram as damping ratio ζ is varied from 0 to 0.15, while the other parameters are fixed at $\mu = 0.1$, $\beta = 0.2$ and $f_0 = 0.2$. The Poincaré map of the stroboscopic time $\Delta\tau = 2\pi\mu$ is used for computing the bifurcation diagram. The zoomed diagram in the 0–0.04 range is shown in Fig. 5b. The blue dots denote forward sweeping results, while the red dots denote backward sweeping results. Sometimes it is difficult to distinguish between chaos and quasi-periodic motion only by bifurcation diagram, but fortunately it has been proved by Levinson [29] that there is no quasi-periodic solution in second-order dynamical system with dissipative damping such as the QZS isolator studied in this paper. And the maximum Lyapunov exponent is also plotted in Fig. 5c to better identify chaos. (Positive maximum Lyapunov exponent implies chaos.) When ζ increases from 0, the chaos arises first and lasts until ζ is increased to 0.0118, where the period-2 solution begins to exist. When the damping ratio increases to 0.0139, the period-halving (PH) bifurcation (also called the reversed period-doubling bifurcation) occurs, which makes the period-2 motion change to period-1 motion. For the backward sweeping ζ , the response is first a period-1 motion when ζ is decreased from 0.15; then, at $\zeta = 0.03457$, the period-1 solution branch begins to deviate from the branch obtained by forward sweeping, due to the symmetry-breaking (SB) bifurcation at this point. (The SB bifurcation is also called the pitchfork bifurcation.) With the further decrease of ζ , the period-doubling (PD) bifurcation occurs at the same ζ value as that of the PH bifurcation, and finally, it becomes the chaos.

Figure 6 depicts the bifurcation diagram as excitation amplitude f_0 is varied, while the other parameters are fixed at $\mu = 0.27$, $\beta = 0.2$ and $\zeta = 0.03$. The forward and backward sweeping bifurcation diagrams are depicted in two panels. With varying the excitation amplitude from $f_0 = 0$, the period-1 solution first

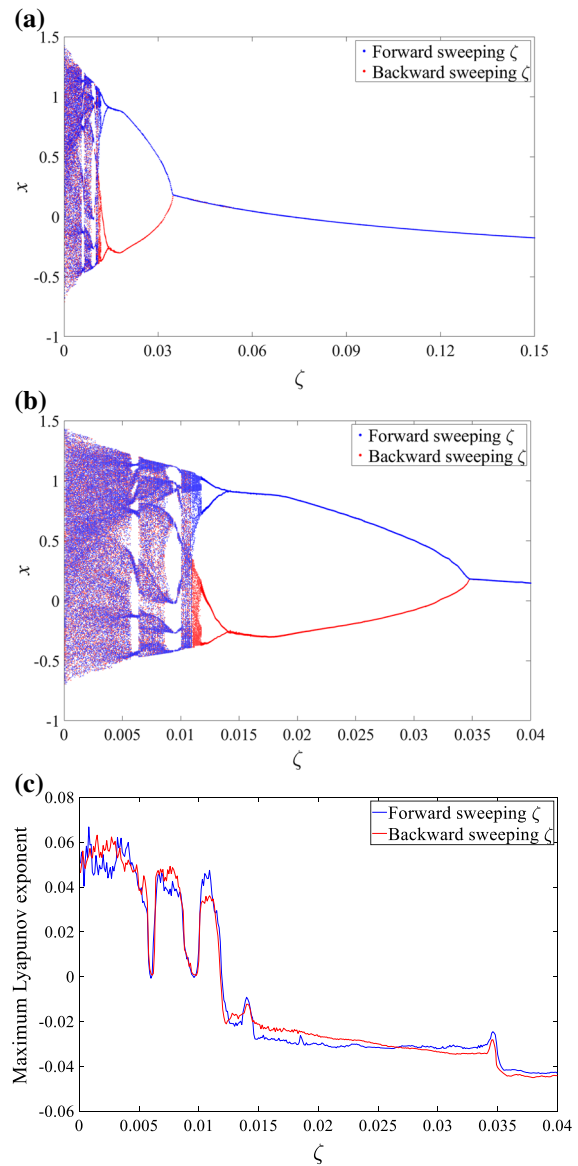


Fig. 5 **a** Bifurcation diagram as ζ is varied ($\mu = 0.1$, $\beta = 0.2$, $f_0 = 0.2$); **b** zoom in 0–0.04 range; **c** maximum Lyapunov exponent in 0–0.04 range

arises and then experiences a jump at $f_0 = 0.0192$, which is essentially caused by the saddle-node (SN) bifurcation. When f_0 is increased to 0.1076, the SB bifurcation occurs, which makes the original period-1 solution become unstable and generates a pair of stable period-1 solution branches. (The forward sweeping solution follows the upper branch, and the backward sweeping solution follows the lower branch.) After experiencing two PD bifurcations successively at

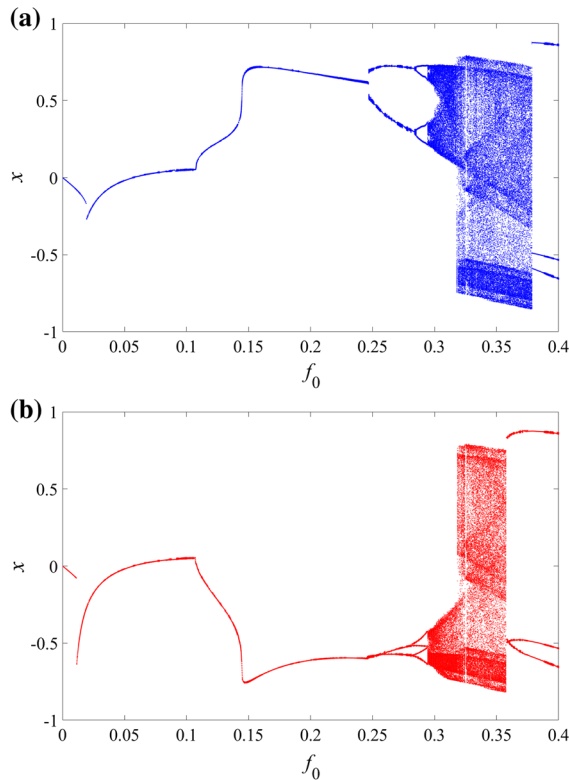


Fig. 6 Bifurcation diagram as f_0 is varied ($\mu = 0.27$, $\beta = 0.2$, $\zeta = 0.03$) **(a)** forward sweeping; **(b)** backward sweeping)

$f_0 = 0.2473$ and $f_0 = 0.2851$, the solution becomes period-4 motion. Then the period-4 motion is changed to the chaotic motion at $f_0 = 0.2946$, and the chaotic state lasts until $f_0 = 0.3785$, where the period-3 motion is generated. The bifurcation pattern of backward sweeping is the same as that of the forward sweeping, but in the reverse direction; besides, for backward sweeping, the point at which period-3 motion becomes chaotic motion (0.3577) and the SN bifurcation point at which jump occurs (0.0114) are smaller than those of the forward sweeping, respectively.

The above bifurcation analyses also indicate that, under different combinations of parameters, the QZS isolator may exhibit various types of response, including period- n ($n = 1, 2, 3, 4$) responses and chaotic response. And there may be coexisting motions under a given parameter condition, but different initial conditions. Figure 7 presents the phase trajectories and attractors of these different response types under different damping ratios and excitation amplitudes, in which the black dashed lines denote coexisting motions.

The triangular points, square points, pentagram points and diamond points denote period-1, period-2, period-3 and period-4 attractors, respectively, and the dots denote chaotic attractors. Figure 7a–f shows the period-1 motion, coexisting period-1 motions, coexisting period-2 motions, coexisting period-4 motions, period-3 motion and chaotic motion, respectively; Fig. 7g shows the coexistence of chaotic motion and period-3 motion; Fig. 7h shows the coexisting chaotic motions.

Figure 8 depicts the $\zeta \sim f_0$ parameter mappings for different response types, which are calculated with the same initial condition $(x(0), x'(0)) = (0, 0)$. The period-1 solution, period-2 solution, period-3 solution, period-4 solution and chaotic solution occur in the cyan region red region, blue region black region and green region, respectively. It can be clearly seen that the period-1 solution occurs in a vast parameter region, whereas the parameter regions for the occurrences of multi-period solutions and chaotic solution are relatively small.

3.2 Further numerical analysis of period-1 response

Since the period-1 solution can occur in a relatively large region of parameter space the following focus is placed on the period-1 solution. To do this, we select a set of parameters that give rise to period-1 solution ($\beta = 0.2$, $\zeta = 0.1$, $f_0 = 0.05$ with μ varying) and then perform detailed numerical simulations. The (steady-state) simulation results at some simulation frequencies are shown in Figs. 9, 10, 11 and 12, including time histories, frequency spectra and phase trajectories. The frequency spectrum and the phase trajectory are derived from the time history.

It can be seen that the period-1 response of the QZS isolator contains not only primary harmonic, but also multiple superharmonics, which validates the existence of superharmonic resonance. The frequencies of these superharmonics are odd times the excitation frequency. Note that in Fig. 12, although the response looks as though it contains only the primary harmonic, the superharmonics do exist with very small amplitudes. For more simulations at other different excitation frequencies, the amplitudes of the harmonics (including primary harmonic and superharmonics) are shown in Fig. 13, in which the superharmonics of order higher than 9 are not presented. Figure 13 indicates that: (a) Theoretically, the superharmonic resonance occurs at

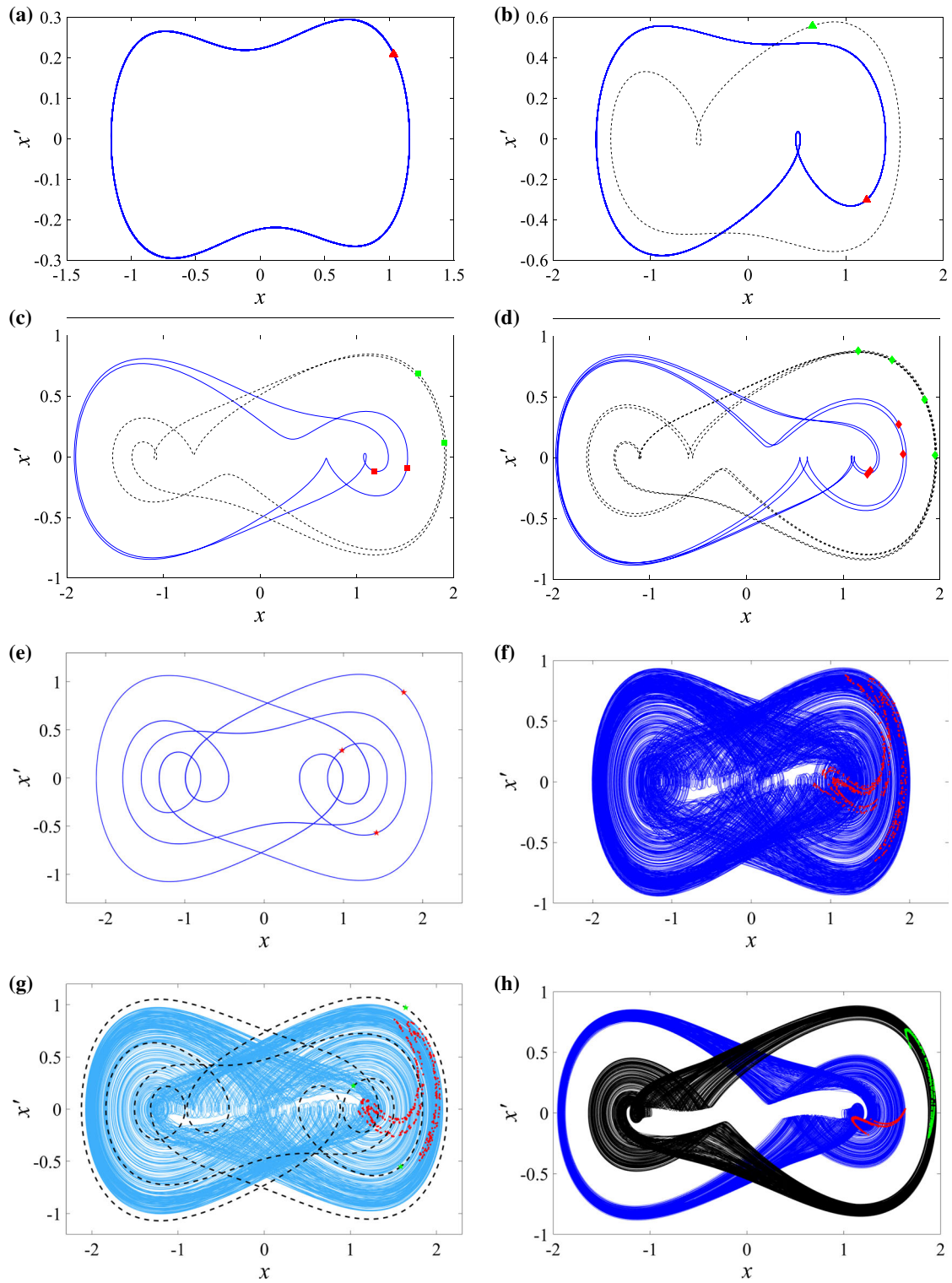


Fig. 7 Phase trajectories and attractors of different response types ($\mu = 0.3, \beta = 0.2$) **(a)** $\zeta = 0.05, f_0 = 0.1$ **(b)** $\zeta = 0.05, f_0 = 0.2$ **(c)** $\zeta = 0.03, f_0 = 0.34$ **(d)** $\zeta = 0.03, f_0 = 0.39$ **(e)** $\zeta = 0.015, f_0 = 0.38$ **(f)** $\zeta = 0.02, f_0 = 0.38$ **(g)** $\zeta = 0.014, f_0 = 0.35$ **(h)** $\zeta = 0.02, f_0 = 0.35$

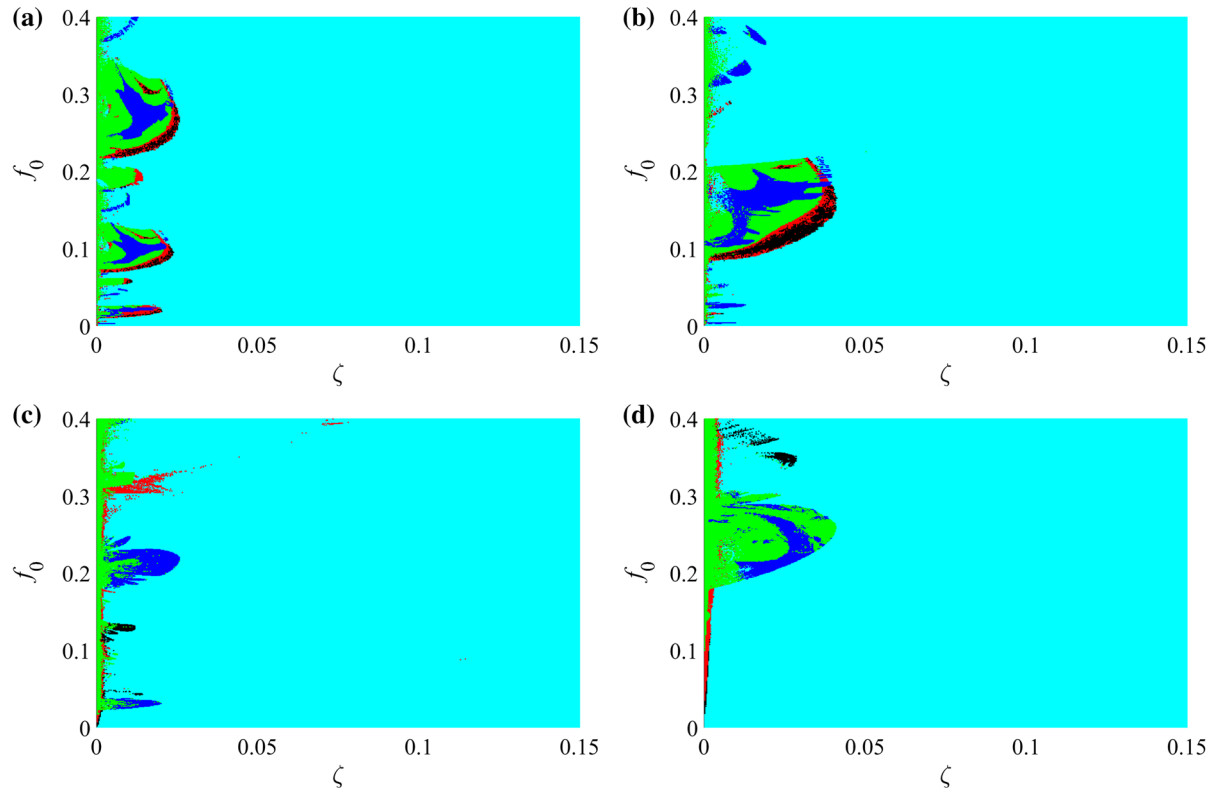


Fig. 8 ζf_0 parameter mappings for different response types ($\beta = 0.2$) **(a** $\mu = 0.1$; **b** $\mu = 0.2$; **c** $\mu = 0.4$; **d** $\mu = 0.8$) (the cyan region, red region, blue region and green

region denote period-1 solution, period-2 solution, period-3 solution, period-4 solution and chaotic solution, respectively). (Color figure online)

any excitation frequency, but it becomes apparent only at relatively low excitation frequencies; (b) when the excitation frequency is higher than a certain value (for example, about 0.35 in Fig. 13), all the superharmonic amplitudes are nearly zero (but not equal to zero), in which case the steady-state response looks like a single harmonic; (c) the superharmonic amplitudes are relatively small compared to the primary harmonic amplitude; and (d) for a given excitation frequency, the superharmonic amplitude generally decreases with the increase in order.

4 Analytical analysis of the superharmonic resonance

4.1 Superharmonic response solution

Since the frequencies of the superharmonics are odd times the excitation frequency, the steady-state response can be assumed to take the following form:

$$x(\tau) = \sum_{n=1}^N A_{2n-1} \cos [(2n-1)\mu\tau + \varphi_{2n-1}] \quad (21)$$

where A_{2n-1} and φ_{2n-1} are the amplitude and phase of each harmonic, respectively, and N is the number of harmonics considered; the highest order of superharmonics in Eq. (21) is $2N - 1$. Before substituting Eq. (21) into Eq. (18), $x^3(\tau)$ is calculated at first:

$$\begin{aligned} x^3(\tau) &= \left\{ A_1 \cos (\mu\tau + \varphi_1) + \sum_{n=2}^N A_{2n-1} \right. \\ &\quad \left. \cos [(2n-1)\mu\tau + \varphi_{2n-1}] \right\}^3 \\ &= A_1^3 \cos^3 (\mu\tau + \varphi_1) + 3A_1^2 \cos^2 (\mu\tau + \varphi_1) \\ &\quad \cdot \sum_{n=2}^N A_{2n-1} \cos [(2n-1)\mu\tau + \varphi_{2n-1}] \\ &\quad + 3A_1 \cos (\mu\tau + \varphi_1) \end{aligned}$$

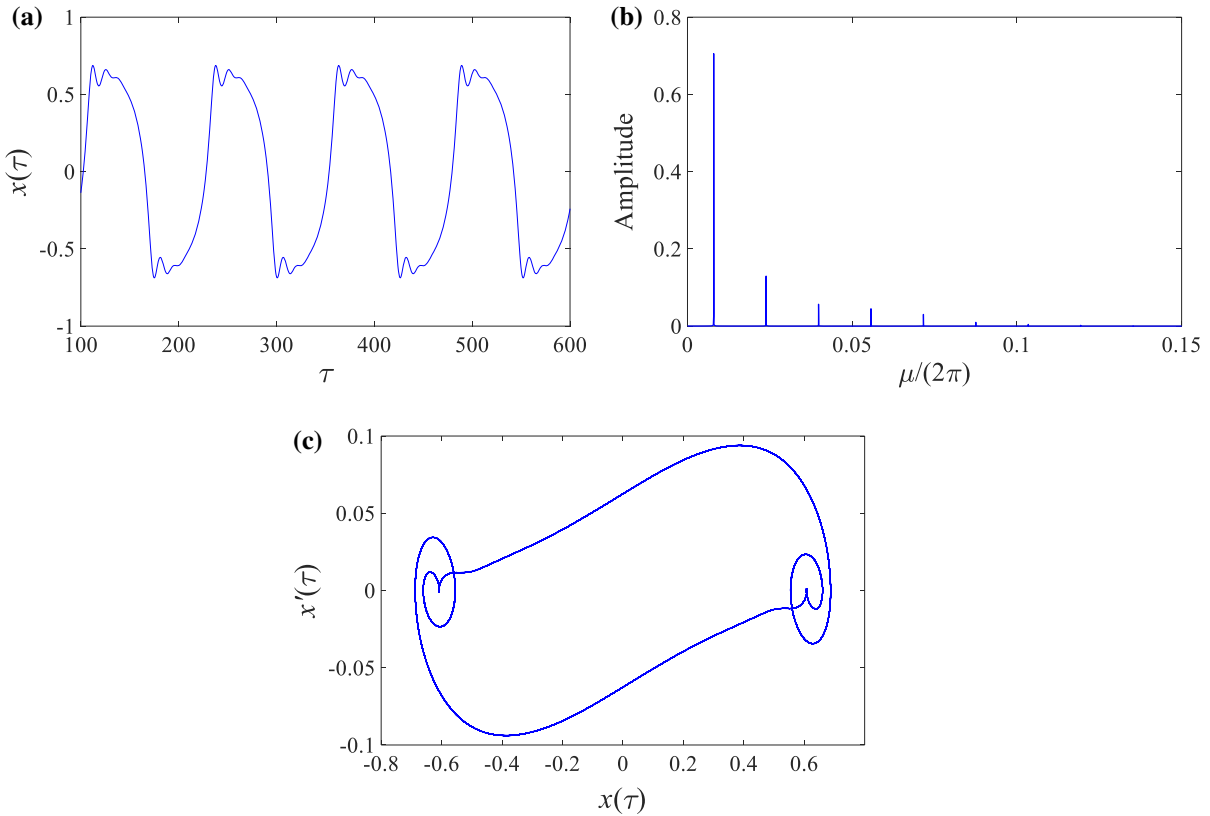


Fig. 9 Numerical results at $\mu = 0.05$ (**a** time history; **b** frequency spectrum; **c** phase trajectory)

$$\begin{aligned} & \cdot \left\{ \sum_{n=2}^N A_{2n-1} \cos[(2n-1)\mu\tau + \varphi_{2n-1}] \right\}^2 \\ & + \left\{ \sum_{n=2}^N A_{2n-1} \cos[(2n-1)\mu\tau + \varphi_{2n-1}] \right\}^3 \end{aligned} \quad (22)$$

Considering that the superharmonic amplitudes ($A_3 \sim A_{2N-1}$) are all small compared to the primary harmonic amplitude (A_1), the higher-order terms of $A_3 \sim A_{2N-1}$ can be ignored, and then, the expansion of $x^3(\tau)$ is simplified as

$$\begin{aligned} x^3(\tau) & \approx A_1^3 \cos^3(\mu\tau + \varphi_1) + 3A_1^2 \cos^2(\mu\tau + \varphi_1) \\ & \cdot \sum_{n=2}^N A_{2n-1} \cos[(2n-1)\mu\tau + \varphi_{2n-1}] \\ & = \frac{3}{4} A_1^2 [A_1 \cos(\mu\tau + \varphi_1) \\ & + A_3 \cos(\mu\tau + \varphi_3 - 2\varphi_1)] \\ & + \frac{1}{4} A_1^2 [A_1 \cos(3\mu\tau + 3\varphi_1) \\ & + 6A_3 \cos(3\mu\tau + \varphi_3)] \end{aligned}$$

$$\begin{aligned} & + 3A_5 \cos(3\mu\tau + \varphi_5 - 2\varphi_1)] \\ & + \frac{3}{4} A_1^2 \cdot \sum_{n=3}^{N-1} \{A_{2n-3} \cos[(2n-1)\mu\tau \\ & + \varphi_{2n-3} + 2\varphi_1]\} \\ & + 2A_{2n-1} \cos[(2n-1)\mu\tau + \varphi_{2n-1}] \\ & + A_{2n+1} \cos[(2n-1)\mu\tau + \varphi_{2n+1} - 2\varphi_1]\} \\ & + \frac{3}{4} A_1^2 \{A_{2N-3} \cos[(2N-1)\mu\tau + \varphi_{2N-3} + 2\varphi_1] \\ & + 2A_{2N-1} \cos[(2N-1)\mu\tau + \varphi_{2N-1}]\} \\ & + \frac{3}{4} A_1^2 A_{2N-1} \cos[(2N+1)\mu\tau + \varphi_{2N-1} + 2\varphi_1] \end{aligned} \quad (23)$$

Substituting Eqs. (21) and (23) into Eq. (18) and equating the coefficients of equivalent harmonics on both sides of the equation give

$$-\mu^2 A_1 + \frac{3}{4} \beta [A_1^3 + A_1^2 A_3 \cos(3\varphi_1 - \varphi_3)] = f_0 \cos \varphi_1 \quad (24a)$$

$$-2\zeta \mu A_1 + \frac{3}{4} \beta A_1^2 A_3 \sin(3\varphi_1 - \varphi_3) = f_0 \sin \varphi_1 \quad (24b)$$

$$\begin{aligned} & -9\mu^2 A_3 + \frac{1}{4} \beta [6A_1^2 A_3 + A_1^3 \cos(\varphi_3 - 3\varphi_1) \\ & + 3A_1^2 A_5 \cos(2\varphi_1 + \varphi_3 - \varphi_5)] = 0 \end{aligned} \quad (24c)$$

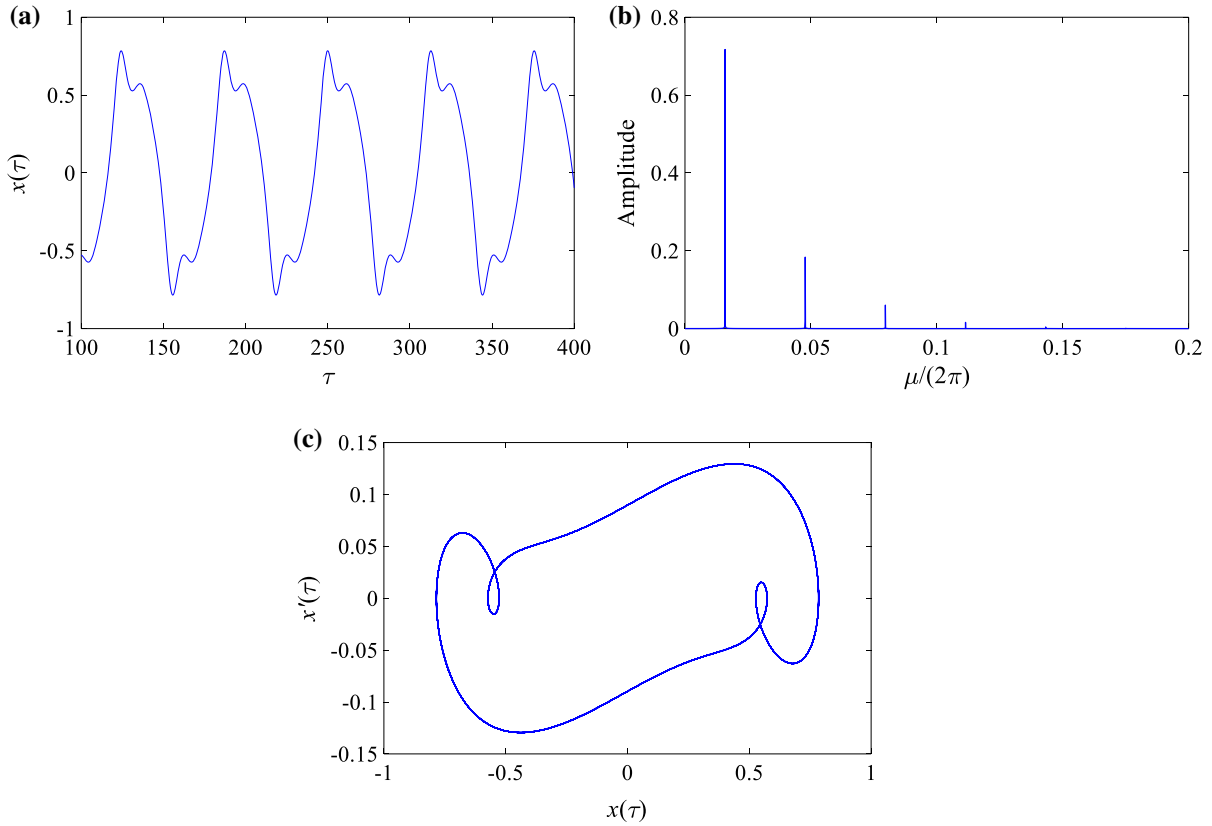


Fig. 10 Numerical results at $\mu = 0.1$ **(a** time history; **b** frequency spectrum; **c** phase trajectory)

$$\begin{aligned} & -6\zeta\mu A_3 + \frac{1}{4}\beta [A_1^3 \sin(\varphi_3 - 3\varphi_1) \\ & + 3A_1^2 A_5 \sin(2\varphi_1 + \varphi_3 - \varphi_5)] = 0 \end{aligned} \quad (24d)$$

$$- (2n-1)^2 \mu^2 A_{2n-1} + \frac{3}{4}\beta A_1^2 [2A_{2n-1}$$

$$+ A_{2n-3} \cos(\varphi_{2n-1} - \varphi_{2n-3} - 2\varphi_1)$$

$$+ A_{2n+1} \cos(\varphi_{2n-1} - \varphi_{2n+1} + 2\varphi_1)] = 0$$

(when $3 \leq n \leq N-1$)

$$- (4n-2)\zeta\mu A_{2n-1} + \frac{3}{4}\beta A_1^2 [A_{2n-3} \sin(\varphi_{2n-1}$$

$$-\varphi_{2n-3} - 2\varphi_1)$$

$$+ A_{2n+1} \sin(\varphi_{2n-1} - \varphi_{2n+1} + 2\varphi_1)] = 0$$

($3 \leq n \leq N-1$)

$$- (2N-1)^2 \mu^2 A_{2N-1} + \frac{3}{4}\beta A_1^2 [2A_{2N-1}$$

$$+ A_{2N-3} \cos(\varphi_{2N-1} - \varphi_{2N-3} - 2\varphi_1)] = 0$$

$$- (4N-2)\zeta\mu A_{2N-1} + \frac{3}{4}\beta A_1^2 A_{2N-3} \sin(\varphi_{2N-1}$$

$$-\varphi_{2N-3} - 2\varphi_1) = 0$$

Solving Eq. (24a) gives the amplitude and phase of each harmonic.

If we only consider the primary resonance and the third-order superharmonic resonance, Eq. (24a) can be much easier, from which a quintic equation in A_1^2 and the expressions of A_3 and $\cos\varphi_1$ depending on A_1 can be derived:

$$\begin{aligned} p_5(\mu) A_1^{10} + p_4(\mu) A_1^8 + p_3(\mu) A_1^6 \\ + p_2(\mu) A_1^4 + p_1(\mu) A_1^2 + p_0(\mu) = 0 \end{aligned} \quad (25)$$

$$A_3 = \frac{\beta A_1^3}{6\sqrt{(\beta A_1^2 - 6\mu^2)^2 + (4\zeta\mu)^2}} \quad (26a)$$

$$\begin{aligned} \cos\varphi_1 = \frac{(3\beta A_1^2 - 4\mu^2) A_1}{4f_0} \\ - \frac{\beta^2 A_1^5 (\beta A_1^2 - 6\mu^2)}{8[(\beta A_1^2 - 6\mu^2)^2 + (4\zeta\mu)^2] f_0} \end{aligned} \quad (26b)$$

where

$$p_5(\mu) = \frac{225}{256}\beta^4 \quad (27a)$$

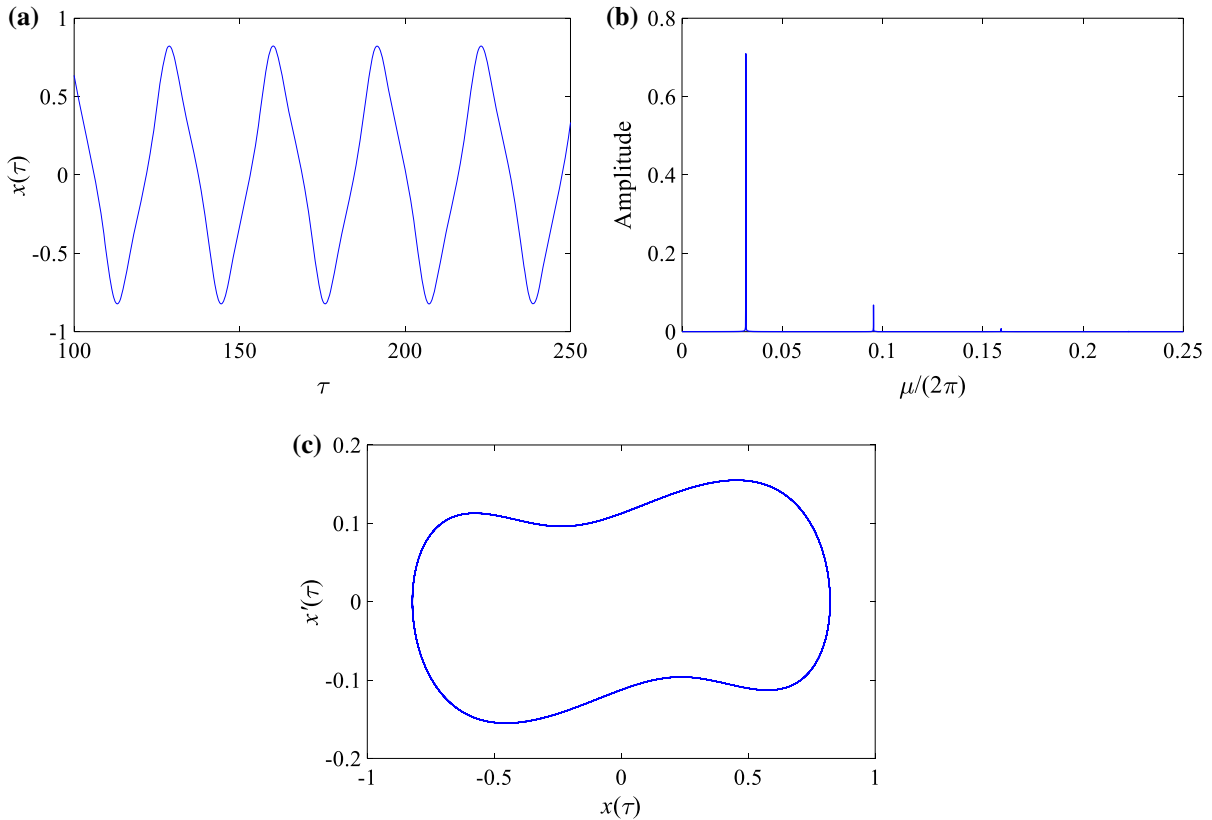


Fig. 11 Numerical results at $\mu = 0.2$ **(a** time history; **b** frequency spectrum; **c** phase trajectory)

$$p_4(\mu) = -\frac{495}{32}\beta^3\mu^2 \quad (27b)$$

$$p_3(\mu) = \frac{9}{4}\beta^2\mu^2 \left(\frac{151}{4}\mu^2 + 15\zeta^2 \right) \quad (27c)$$

$$p_2(\mu) = -\beta\mu^4 \left(\frac{297}{2}\mu^2 + 162\zeta^2 \right) - \frac{9}{4}\beta^2f_0^2 \quad (27d)$$

$$p_1(\mu) = 9\mu^4 \left(9\mu^2 + 4\zeta^2 \right) \left(\mu^2 + 4\zeta^2 \right) + 27\beta\mu^2f_0^2 \quad (27e)$$

$$p_0(\mu) = -9\mu^2 \left(9\mu^2 + 4\zeta^2 \right) f_0^2 \quad (27f)$$

Figure 14 shows the analytical (non-dimensional) amplitude–frequency curves of primary resonance and third-order superharmonic resonance under different excitation amplitudes, and the primary harmonic amplitude and third-order harmonic amplitude obtained by numerical simulations are also presented for comparison. The other two parameters are fixed at $\beta = 0.2$ and $\zeta = 0.1$. It can be seen that the analytical solutions are in good agreement with the numerical solutions; there only exists a little gap between

the analytical and numerical solutions at low excitation frequencies. The primary harmonic amplitude–frequency curve has a valley and two peaks, while the third-order harmonic amplitude–frequency curve only has a peak; the frequency at the peak of the third-order harmonic amplitude curve almost coincides with that at the valley of the primary harmonic amplitude curve. There is a narrow frequency range in which the primary harmonic amplitude decreases rapidly and the third-order harmonic amplitude decreases to nearly zero; in the lower-frequency range, the third-order superharmonic resonance is comparatively apparent; in the higher-frequency range, the third-order harmonic amplitude is almost kept at zero, and the primary harmonic amplitude keeps decreasing and will gradually approach zero. As the excitation amplitude increases, the frequency at which the third harmonic amplitude decreases to nearly zero is increased, and all the peaks and valley on the amplitude curves are moved to the right. When the excitation amplitude is increased to a certain degree, a frequency range in which three analyt-

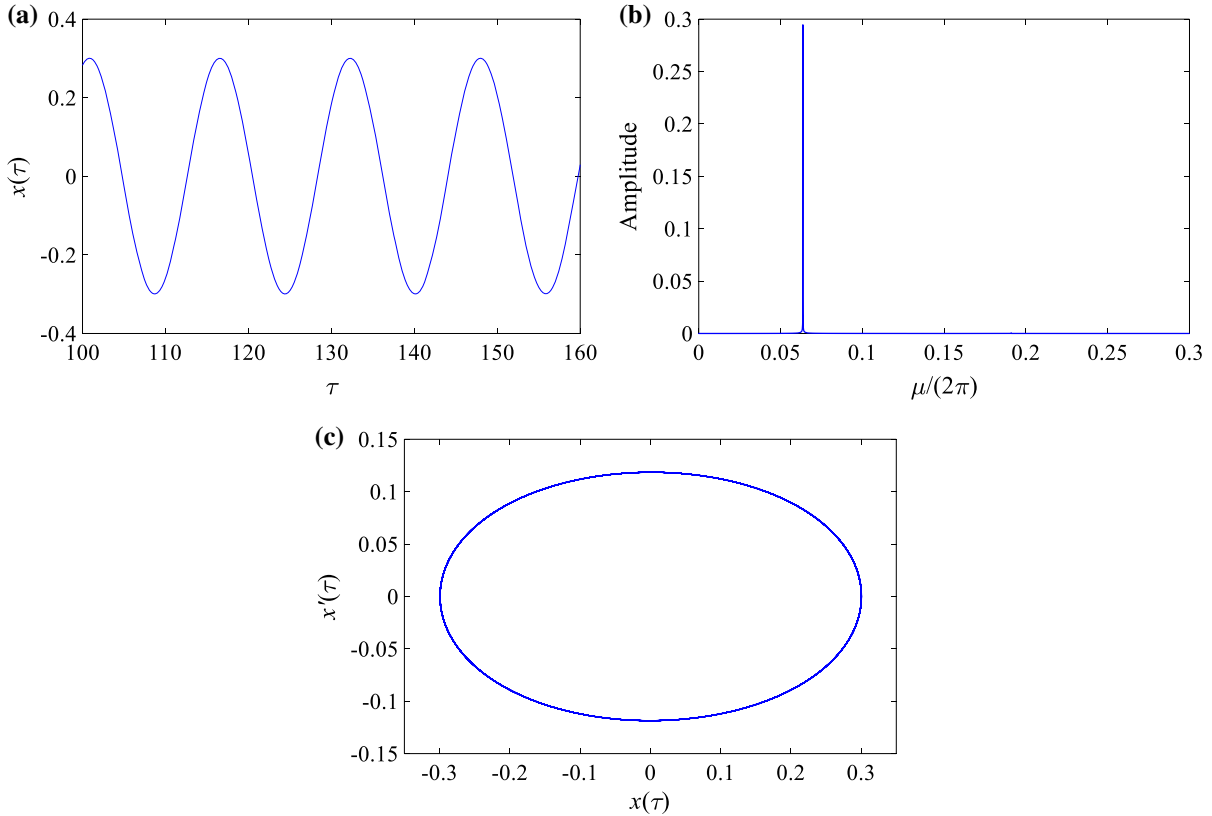


Fig. 12 Numerical results at $\mu = 0.4$ (**a** time history; **b** frequency spectrum; **c** phase trajectory)

ical solutions coexist appears, which will cause jump phenomenon; in this frequency range, which of these solutions represents the actual solution depends on the initial condition. The response amplitude calculated under single-harmonic response assumption (by following the procedure in previous works such as Refs. [5, 7, 13, 18]) is also plotted in Fig. 14 (red dotted lines) for comparison. It can be seen that, at high frequencies, the response amplitude calculated under single-harmonic response assumption is almost equal to the primary resonance amplitude; the reason for this is that at high frequencies the superharmonic components are very small.

4.2 Stability analysis

For the sake of completeness, a semi-analytical method is employed to determine the stable region. Assuming that the response given by Eq. (21) is disturbed by a small perturbation ε , the response of the system becomes

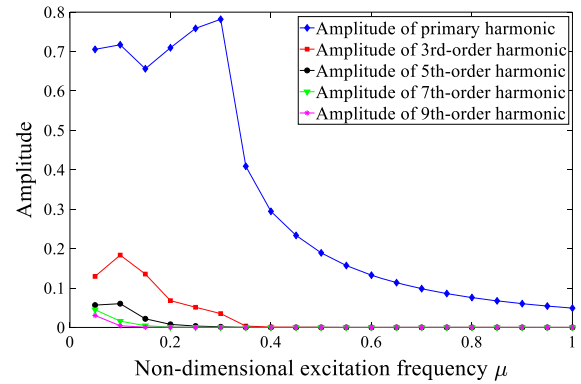


Fig. 13 Simulated primary harmonic amplitude and superharmonic amplitudes at different excitation frequencies

$$x(\tau) = \bar{x}(\tau) + \varepsilon(\tau) \quad (28)$$

where $\bar{x}(\tau) = \sum_{n=1}^N A_{2n-1} \cos[(2n-1)\mu\tau + \varphi_{2n-1}]$ is the undisturbed response. Substituting Eq. (28) into the equation of motion Eq. (18) gives

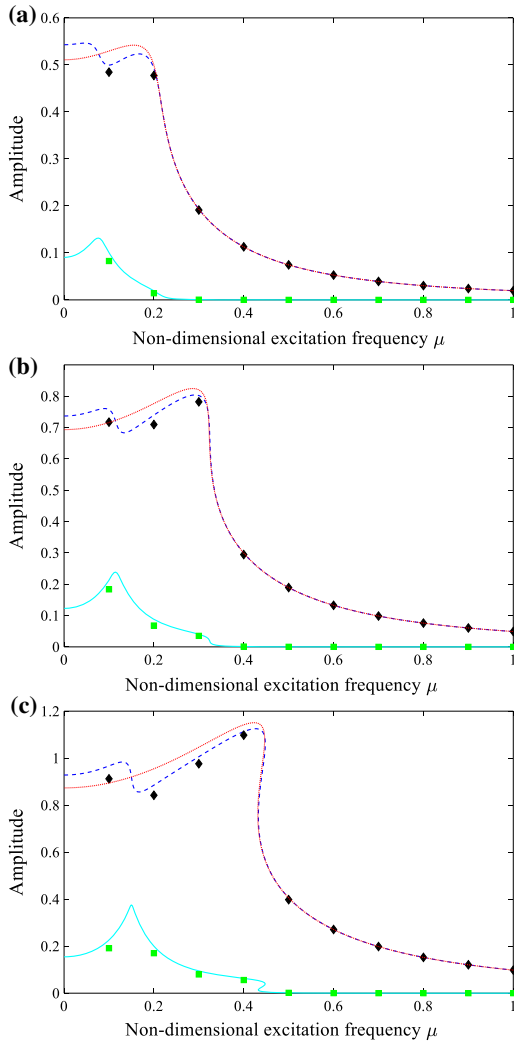


Fig. 14 Analytical and simulated primary harmonic amplitudes and third-order harmonic amplitudes, and the amplitude calculated under single-harmonic response assumption (**a** $f_0 = 0.02$; **b** $f_0 = 0.05$; **c** $f_0 = 0.1$) (blue dashed lines show the analytical primary harmonic amplitude; cyan solid lines show the analytical third-order harmonic amplitude; black rhombuses show the simulated primary harmonic amplitude; green squares show the simulated third-order harmonic amplitude; and red dotted lines show the amplitude calculated under single-harmonic response assumption). (Color figure online)

$$(\bar{x} + \varepsilon)'' + 2\zeta(\bar{x} + \varepsilon)' + \beta(\bar{x} + \varepsilon)^3 = f_0 \cos(\mu\tau) \quad (29)$$

Since $\bar{x}(\tau)$ is the undisturbed response, $\bar{x}'' + 2\zeta\bar{x}' + \beta\bar{x}^3 = f_0 \cos(\mu\tau)$ can definitely be satisfied. Comparing this equation with Eq. (29) and neglecting higher-order terms of ε result in a linear ordinary differential

equation with periodically varying coefficient:

$$\varepsilon'' + 2\zeta\varepsilon' + \rho(\tau)\varepsilon = 0 \quad (30)$$

where

$$\begin{aligned} \rho(\tau) &= 3\beta \left\{ A_1 \cos(\mu\tau + \varphi_1) + \sum_{n=2}^N A_{2n-1} \right. \\ &\quad \left. \cos[(2n-1)\mu\tau + \varphi_{2n-1}] \right\}^2 \\ &\approx 3\beta \left\{ A_1^2 \cos^2(\mu\tau + \varphi_1) + 2A_1 \cos(\mu\tau + \varphi_1) \right. \\ &\quad \left(\sum_{n=2}^N A_{2n-1} \cos[(2n-1)\mu\tau + \varphi_{2n-1}] \right) \Big\} \\ &= 3\beta \left\{ \frac{A_1^2}{2} + \frac{A_1^2}{2} \cos(2\mu\tau + 2\varphi_1) \right. \\ &\quad \left. + A_1 \sum_{n=2}^N A_{2n-1} [\cos((2n-2)\mu\tau + \varphi_{2n-1} - \varphi_1) \right. \\ &\quad \left. + \cos(2n\mu\tau + \varphi_{2n-1} + \varphi_1)] \right\} \end{aligned} \quad (31)$$

Equation (30) is called the perturbation equation. On the one hand, in Eq. (24a), superharmonic amplitudes appear in the form of first order, so they can be expressed as functions of the primary harmonic amplitude; on the other hand, since $\rho(\tau)$ is a periodic function, the initial phase does not influence the convergence or divergence of $\varepsilon(\tau)$ and thus is insignificant. Therefore, the expression of $\rho(\tau)$ can be considered to depend on the primary harmonic amplitude A_1 and the (non-dimensional) excitation frequency μ .

Considering that the perturbation equation Eq. (30) is a second-order linear ordinary differential equation, there exist two linearly independent solutions, which are denoted as $q_1(\tau)$ and $q_2(\tau)$, and any of the solutions that satisfy the perturbation equation can be expressed as follows:

$$\varepsilon(\tau) = a_1 q_1(\tau) + a_2 q_2(\tau) \quad (32)$$

where a_1 and a_2 depend on the initial condition $(\varepsilon(0), \varepsilon'(0))$. Equation (31) shows that ρ/τ is a periodic function with a period of π/μ , i.e., $\rho/(\tau + \pi/\mu) = \rho(\tau)$. Therefore, now that $q_1(\tau)$ and $q_2(\tau)$ satisfy

the perturbation equation, $q_1(\tau + \pi/\mu)$ and $q_2(\tau + \pi/\mu)$ must also satisfy the perturbation equation. Then, $q_1(\tau + \pi/\mu)$ and $q_2(\tau + \pi/\mu)$ can be expressed as $q_1(\tau + \pi/\mu) = G_{11}q_1(\tau) + G_{21}q_2(\tau)$ and $q_2(\tau + \pi/\mu) = G_{12}q_1(\tau) + G_{22}q_2(\tau)$, i.e.,

$$\left[q_1\left(\tau + \frac{\pi}{\mu}\right), q_2\left(\tau + \frac{\pi}{\mu}\right) \right] = [q_1(\tau), q_2(\tau)] \mathbf{G} \quad (33)$$

where $[q_1(\tau), q_2(\tau)]$ is called the fundamental solution vector and $\mathbf{G}_{2 \times 2}$ is called the characteristic matrix hereafter. Although the characteristic matrix is dependent on the choice of fundamental solution vector, its eigenvalues are unique and thus can reflect the inherent characteristics of the perturbation equation. The uniqueness of the eigenvalues is proved as follows: Introduce another fundamental solution vector $[\tilde{q}_1(\tau), \tilde{q}_2(\tau)]$ and its corresponding characteristic matrix $\tilde{\mathbf{G}}$, and then, we have

$$\left[\tilde{q}_1\left(\tau + \frac{\pi}{\mu}\right), \tilde{q}_2\left(\tau + \frac{\pi}{\mu}\right) \right] = [\tilde{q}_1(\tau), \tilde{q}_2(\tau)] \tilde{\mathbf{G}} \quad (34)$$

According to Eq. (32), $\tilde{q}_1(\tau)$ and $\tilde{q}_2(\tau)$ can be expressed as $\tilde{q}_1(\tau) = C_{11}q_1(\tau) + C_{21}q_2(\tau)$ and $\tilde{q}_2(\tau) = C_{12}q_1(\tau) + C_{22}q_2(\tau)$, i.e.,

$$[\tilde{q}_1(\tau), \tilde{q}_2(\tau)] = [q_1(\tau), q_2(\tau)] \mathbf{C} \quad (35)$$

and therefore

$$\begin{aligned} & \left[\tilde{q}_1\left(\tau + \frac{\pi}{\mu}\right), \tilde{q}_2\left(\tau + \frac{\pi}{\mu}\right) \right] \\ &= \left[q_1\left(\tau + \frac{\pi}{\mu}\right), q_2\left(\tau + \frac{\pi}{\mu}\right) \right] \mathbf{C} \end{aligned} \quad (36)$$

Combining Eqs. (33)–(36) gives

$$[q_1(\tau), q_2(\tau)] \mathbf{G} \mathbf{C} = [q_1(\tau), q_2(\tau)] \mathbf{C} \tilde{\mathbf{G}} \quad (37)$$

Since $[q_1(\tau), q_2(\tau)]$ is variable with respect to the non-dimensional time τ , Eq. (37) implies $\mathbf{G} \mathbf{C} = \mathbf{C} \tilde{\mathbf{G}}$, i.e.,

$$\tilde{\mathbf{G}} = \mathbf{C}^{-1} \mathbf{G} \mathbf{C} \quad (38)$$

which shows that \mathbf{G} and $\tilde{\mathbf{G}}$ are similar matrices to each other, so they have the same eigenvalues; in

other words, the eigenvalues of characteristic matrix are unique and thus can reflect the inherent characteristics of the perturbation equation. Therefore, whether the solution of the perturbation equation diverges or converges is related to the eigenvalues. To proceed, we can construct two solutions using Eq. (32) as follows:

$$\varepsilon_i(\tau) = [q_1(\tau), q_2(\tau)] \mathbf{g}_i \quad (i = 1, 2) \quad (39)$$

where \mathbf{g}_i is the i th ($i = 1, 2$) eigenvector of matrix \mathbf{G} . Then

$$\begin{aligned} \varepsilon_i\left(\tau + \frac{\pi}{\mu}\right) &= \left[q_1\left(\tau + \frac{\pi}{\mu}\right), q_2\left(\tau + \frac{\pi}{\mu}\right) \right] \mathbf{g}_i \\ &= [q_1(\tau), q_2(\tau)] \mathbf{G} \mathbf{g}_i \\ &= \eta_i [q_1(\tau), q_2(\tau)] \mathbf{g}_i \\ &= \eta_i \varepsilon_i(\tau) \quad (i = 1, 2) \end{aligned} \quad (40)$$

where η_i is the i th ($i = 1, 2$) eigenvalue of matrix \mathbf{G} . According to η_i , there are three situations: (1) If $|\eta_i| < 1$, then $\lim_{\tau \rightarrow \infty} \varepsilon_i(\tau) = 0$, which means that the perturbation is convergent; (2) if $|\eta_i| = 1$, then $\lim_{\tau \rightarrow \infty} \varepsilon_i(\tau)$ is bounded, which also means that the perturbation is convergent (but not asymptotically convergent); and (3) if $|\eta_i| > 1$, then $\lim_{\tau \rightarrow \infty} \varepsilon_i(\tau) = \infty$, which means that the perturbation is divergent. Only when both $|\eta_1|$ and $|\eta_2|$ are no larger than unity, the undisturbed response $\bar{x}(\tau)$ is stable; when any of them is larger than unity, the undisturbed response $\bar{x}(\tau)$ is unstable. The eigenvalues of the characteristic matrix are solved by $\det(\mathbf{G} - \eta \mathbf{I}) = 0$, which gives

$$\eta_{1,2} = \frac{\text{tr}(\mathbf{G}) \pm \sqrt{[\text{tr}(\mathbf{G})]^2 - 4 \det(\mathbf{G})}}{2} \quad (41)$$

Differentiating Eq. (33) with the non-dimensional time τ gives $[q'_1(\tau + \pi/\mu), q'_2(\tau + \pi/\mu)] = [q'_1(\tau), q'_2(\tau)] \mathbf{G}$; then, we have

$$\begin{bmatrix} q_1(\tau + \pi/\mu) q_2(\tau + \pi/\mu) \\ q'_1(\tau + \pi/\mu) q'_2(\tau + \pi/\mu) \end{bmatrix} = \begin{bmatrix} q_1(\tau) q_2(\tau) \\ q'_1(\tau) q'_2(\tau) \end{bmatrix} \mathbf{G} \quad (42)$$

As mentioned earlier, although \mathbf{G} depends on the choices of $q_1(\tau)$ and $q_2(\tau)$ and thus is not unique, η_i ($i = 1, 2$) is unique. Therefore, we can use a simple fundamental solution vector and calculate its corresponding characteristic matrix to find the eigenvalues.

Assume that the initial conditions of the fundamental solution vector are

$$\begin{cases} q_1(0) = 1, & q'_1(0) = 0 \\ q_2(0) = 0, & q'_2(0) = 1 \end{cases} \quad (43)$$

then we have

$$\begin{aligned} \mathbf{G} &= \begin{bmatrix} q_1(0) & q_2(0) \\ q'_1(0) & q'_2(0) \end{bmatrix}^{-1} \begin{bmatrix} q_1\left(\frac{\pi}{\mu}\right) & q_2\left(\frac{\pi}{\mu}\right) \\ q'_1\left(\frac{\pi}{\mu}\right) & q'_2\left(\frac{\pi}{\mu}\right) \end{bmatrix} \\ &= \begin{bmatrix} q_1\left(\frac{\pi}{\mu}\right) & q_2\left(\frac{\pi}{\mu}\right) \\ q'_1\left(\frac{\pi}{\mu}\right) & q'_2\left(\frac{\pi}{\mu}\right) \end{bmatrix} \end{aligned} \quad (44)$$

It can be seen that $\det(\mathbf{G})$ is actually the Wronskian determinant at $\tau = \pi/\mu$; therefore, based on the well-known Liouville formula, we have

$$\begin{aligned} \det(\mathbf{G}) &= \det\left(\begin{bmatrix} q_1(0) & q_2(0) \\ q'_1(0) & q'_2(0) \end{bmatrix}\right) \cdot \exp\left\{-\int_0^{\pi/\mu} 2\xi d\tau\right\} \\ &= e^{-2\xi\pi/\mu} \end{aligned} \quad (45)$$

It can be calculated from Eq. (41) that, in the case of $\det(\mathbf{G}) = e^{-2\xi\pi/\mu} < 1$, the condition for $|\eta_{1,2}| \leq 1$ is $|\text{tr}(\mathbf{G})| \leq 1 + e^{-2\xi\pi/\mu}$, i.e.,

$$\left|q_1\left(\frac{\pi}{\mu}\right) + q'_2\left(\frac{\pi}{\mu}\right)\right| \leq 1 + e^{-2\xi\pi/\mu} \quad (46)$$

This inequality is thus the condition that gives rise to stability.

Next, based on the stability criterion given in Eq. (46), we need to employ numerical means to obtain the stable region: For each combination of A_1 and μ , which can determine the expression of $\rho(\tau)$ (the reason has been explained earlier), we conduct time integration using the perturbation equation Eq. (30) with the initial conditions given in Eq. (43) to derive $q_1(\pi/\mu)$ and $q'_2(\pi/\mu)$ and see whether Eq. (46) can be satisfied; if so, this combination of A_1 and μ is stable. By repeating this process using many different combinations of A_1 and μ , the stable region in (A_1, μ) plane can be obtained. Based on the relationship between A_1 and A_n ($n = 2 \sim N$), the stable region in (A_n, μ) plane can also be obtained.

Figure 15 shows the unstable regions of the primary resonance (pink region) and the third-order superharmonic resonance (light green region); the amplitude-frequency curves of the primary resonance (blue lines) and the third-order superharmonic resonance (red lines)

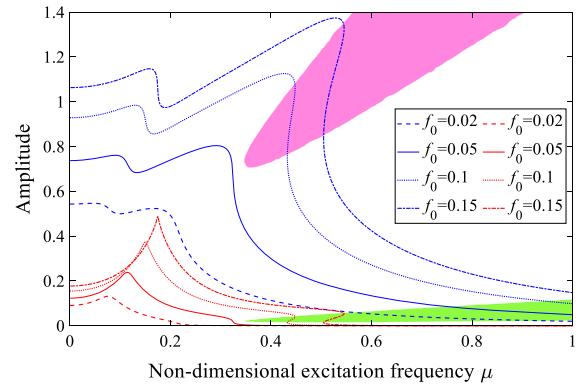


Fig. 15 Unstable regions of the primary resonance (pink region) and the third-order superharmonic resonance (light green region) ($\beta = 0.2$, $\zeta = 0.1$). (Color figure online)

under different excitation amplitudes are also shown for examination. It can be seen that when there is no jump phenomenon, the whole amplitude–frequency curve is stable; when the jump phenomenon exists, the upper and lower solution branches are stable, while the intermediate solution branch is unstable.

4.3 Superharmonic energy factor

There are multiple superharmonics in the response. In order to consider these superharmonics from a global perspective, it is necessary to introduce an index to characterize their overall properties. It is well known that root-mean-square (RMS) value can reveal the information about the energy of a signal, so we can find this index from the viewpoint of energy. The RMS of the (non-dimensional) steady-state response of the QZS isolator is

$$R_{\text{QZS}} = \sqrt{\frac{\mu}{2\pi} \int_0^{\frac{2\pi}{\mu}} \left\{ \sum_{n=1}^N A_{2n-1} \cos[(2n-1)\mu\tau + \varphi_{2n-1}] \right\}^2 d\tau} \quad (47)$$

Due to the orthogonality of trigonometric function, Eq. (47) is calculated as

$$R_{\text{QZS}} = \sqrt{\left(\sum_{n=1}^N A_{2n-1}^2 \right)/2} \quad (48)$$

Similarly, the RMS of all of the superharmonics is

$$R_{\text{super}} = \sqrt{\left(\sum_{n=2}^N A_{2n-1}^2 \right) / 2} \quad (49)$$

The *superharmonic energy factor* σ is proposed in this paper to characterize the energy proportion of the superharmonics, which is defined as the ratio of the RMS of the superharmonics to that of the steady-state response:

$$\sigma = \frac{R_{\text{super}}}{R_{\text{QZS}}} = \sqrt{\frac{\sum_{n=2}^N A_{2n-1}^2}{\sum_{n=1}^N A_{2n-1}^2}} = \sqrt{1 - \frac{A_1^2}{\sum_{n=1}^N A_{2n-1}^2}} \quad (50)$$

For given parameters, the superharmonic energy factor varies with the excitation frequency. In Figs. 16, 17 and 18, the superharmonic energy factor is plotted versus non-dimensional excitation frequency under different parameter conditions. The superharmonic energy factor curve presents the variation of the superharmonic energy proportion with respect to the excitation frequency. It can be seen that the superharmonic energy factor σ is increased first and then decreased when increasing the excitation frequency; at high frequencies, the superharmonic energy factor is decreased to nearly zero. This means that the superharmonic energy exists mainly under low-frequency excitation, which is consistent with the findings in previous sections. Roughly speaking, there seems to be a “superharmonic region,” namely the excitation frequency range outside which the superharmonic energy proportion is close to zero.

The superharmonic resonance characteristics of the QZS isolator are related to three parameters (β , ζ and f_0). The superharmonic energy factor curves in each one of Figs. 16, 17 and 18 are plotted by setting two parameters fixed and varying one parameter, and thus can also show the effect of each parameter on the superharmonic energy proportion. The effect of β is very similar to that of f_0 : With the increase of β or f_0 , the maximal superharmonic energy factor and its corresponding frequency are all increased, and the “superharmonic region” is widened; when β or f_0 is increased to a certain degree, the multi-solution phenomenon occurs. The increase of ζ causes the maxi-

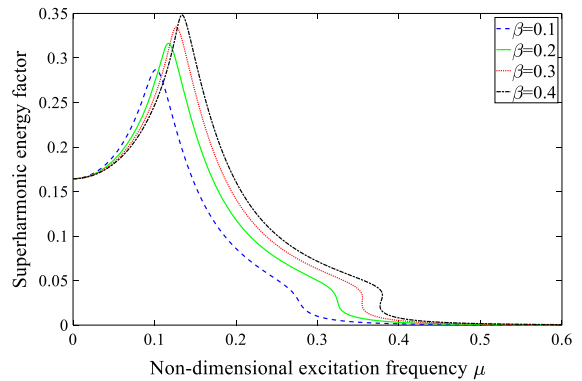


Fig. 16 Superharmonic energy factor versus excitation frequency under different values of β ($\zeta = 0.1$, $f_0 = 0.05$)

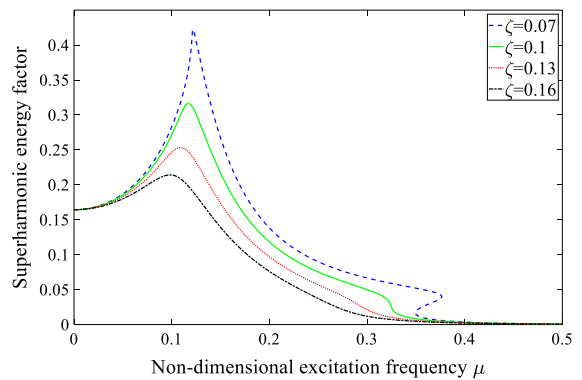


Fig. 17 Superharmonic energy factor versus excitation frequency under different values of ζ ($\beta = 0.2$, $f_0 = 0.05$)

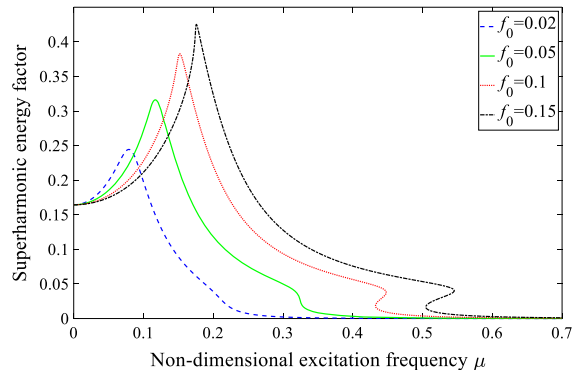


Fig. 18 Superharmonic energy factor versus excitation frequency under different values of f_0 ($\beta = 0.2$, $\zeta = 0.1$)

mal superharmonic energy factor to decrease and narrows the “superharmonic region.” If ζ is too small, the multi-solution phenomenon will also occur. Generally speaking, reducing nonlinear coefficient β or excita-

tion amplitude f_0 , or increasing damping ratio ζ , is conducive to weakening the superharmonic resonance.

The “superharmonic region” is a very important concept which represents the excitation frequency range where the superharmonic resonance perceptibly exists, considering that the superharmonic resonance at the excitation frequencies outside the “superharmonic region” is very small and thus can be disregarded. However, “superharmonic region” is only a qualitative statement; in order to quantitatively describe it, we need to introduce a quantitative index. It can be seen that the “superharmonic region” is from zero frequency to a critical frequency at which the superharmonic energy factor decreases to nearly zero. Therefore, it is sensible to employ this critical frequency as an indicator of the width and location of the “superharmonic region”; this critical frequency is called the *superharmonic truncation frequency* (STF) hereinafter. The next thing is to give a mathematical definition of the superharmonic truncation frequency.

In this paper, the definition of the superharmonic truncation frequency is divided into two categories: (a) When there is no jump phenomenon, the (non-dimensional) superharmonic truncation frequency is defined as the largest one of the (non-dimensional) frequencies at which the second derivative of σ with respect to μ takes local maximum (in fact, in most cases, the second derivative has only one local maximum), or in other words, defined as the largest one of zero points of the third derivative of σ with respect to μ ; (b) when the jump phenomenon occurs, the superharmonic truncation frequency is defined as the jump-down frequency. Figure 19 shows the relationship between the non-dimensional superharmonic truncation frequency and each of the three parameters (β , ζ and f_0). The superharmonic truncation frequency is increased with the increase of β and f_0 , and is decreased with the increase of ζ . Under very light damping, the superharmonic truncation frequency is much more sensitive to the variation in ζ value.

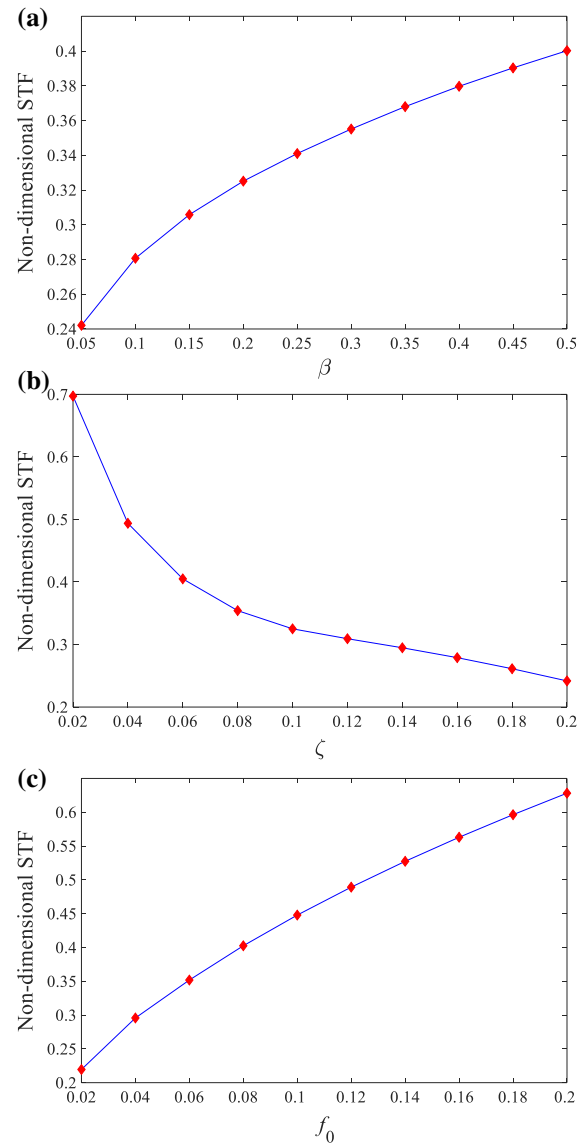


Fig. 19 Relationship between the non-dimensional superharmonic truncation frequency and each parameter (a non-dimensional STF versus β when $\zeta = 0.1$, $f_0 = 0.05$) (b non-dimensional STF versus ζ when $\beta = 0.2$, $f_0 = 0.05$) (c non-dimensional STF versus f_0 when $\beta = 0.2$, $\zeta = 0.1$)

$$F_T(t) = c\dot{X} + F_{QZS}(X) = F(t) - m\ddot{X} \quad (51)$$

5 Effect of superharmonic resonance on the isolation performance

The equation of motion under harmonic force excitation is shown in Eq. (15), from which it can be seen that the force transmitted to the base is

Vibration isolation performance under force excitation is quantified by force transmissibility. In previous studies, the force transmissibility is defined as the ratio of the amplitude of the force transmitted to the base to that of the excitation force, which is based on the assumption that the steady-state response contains only one

harmonic at the excitation frequency, and therefore, the force transmitted to the base is also a single-harmonic signal. However, this definition is no longer applicable when taking multiple superharmonics into account. In this paper, we derive the force transmissibility from the energy perspective, which is defined as the ratio of the RMS of the force transmitted to the base to that of the excitation force:

$$\begin{aligned} T &= \frac{\text{RMS}[F(t) - m\ddot{X}]}{\text{RMS}[F(t)]} = \frac{\text{RMS}[f_0 \cos(\mu\tau) - x'']}{\text{RMS}[f_0 \cos(\mu\tau)]} \\ &= \frac{\sqrt{\frac{\mu}{2\pi} \int_0^{\frac{2\pi}{\mu}} \left\{ f_0 \cos(\mu\tau) + \mu^2 \sum_{n=1}^N (2n-1)^2 A_{2n-1} \cos[(2n-1)\mu\tau + \varphi_{2n-1}] \right\}^2 d\tau}}{\sqrt{\frac{\mu}{2\pi} \int_0^{\frac{2\pi}{\mu}} [f_0 \cos(\mu\tau)]^2 d\tau}} \end{aligned} \quad (52)$$

Calculation of Eq. (52) gives the expression of the force transmissibility

$$T = \frac{\sqrt{f_0^2 + 2\mu^2 A_1 f_0 \cos \varphi_1 + \mu^4 \sum_{n=1}^N (2n-1)^4 A_{2n-1}^2}}{f_0} \quad (53)$$

where A_{2n-1} and $\cos \varphi_1$ are solved from Eq. (24a). It can be seen that if the superharmonic amplitudes in Eq. (53) are set to zero, Eq. (53) would be the same as the force transmissibility expression in the previous literature. In fact, Eq. (53) can be seen as a generalized force transmissibility expression; the expression in the previous literature is actually a particular case of Eq. (53) when assuming that the response is a single-harmonic oscillation.

Figure 20 shows the transmissibility plotted versus the non-dimensional excitation frequency under different values of damping ratio and excitation amplitude in which the transmissibility takes the decibel form (T (dB) = 20lg T). The (decibel form) transmissibility curves calculated under single-harmonic response assumption (by following the procedure in previous works such as Refs. [5, 7, 13, 18]) are also presented in Fig. 20 for comparison, which is given by

$$T_{\text{SHRA}} = \sqrt{\left(\frac{\mu H}{f_0}\right)^2 \left(\frac{3}{2}\beta H^2 - \mu^2\right) + 1} \quad (54)$$

where the subscript “SHRA” denotes “single-harmonic response assumption,” and H is seen as the non-dimensional steady-state response amplitude and break solved from

$$\frac{9}{16}\beta^2 H^6 - \frac{3}{2}\beta\mu^2 H^4 + \mu^2 (\mu^2 + 4\zeta^2) H^2 - f_0^2 = 0 \quad (55)$$

It should be noted that H is different from the primary resonance amplitude A_1 in terms of both meaning and value, which has been illustrated in Fig. 14.

For the convenience of description, the frequency above which isolation can occur is called the *isolation frequency*; the frequency and transmissibility at the peak of the transmissibility curve are called the *peak frequency* and *peak transmissibility*, respectively [3]. The isolation frequency is equal to the frequency at which the transmissibility drops below unity if there is no jump phenomenon, and is equal to the jump-down frequency if the jump phenomenon exists. The effects of damping ratio and excitation amplitude on the transmissibility have been documented in many articles and are not discussed in detail in this paper. In short, increasing ζ results in a decrease in the low-frequency transmissibility, but an increase in the high-frequency transmissibility; increasing f_0 causes the peak transmissibility, peak frequency and isolation frequency to increase. The following discussion focuses on the effect of the superharmonic resonance on the vibration isolation performance, or in other words focuses on the difference between the transmissibility calculated with consideration of superharmonic resonance and the transmissibility calculated under single-harmonic response assumption.

Figure 20 shows that the consideration of the superharmonic resonance brings an increase to the transmissibility; that is, the vibration isolation performance is degraded by the superharmonic resonance. The following questions are the frequency range of influence and

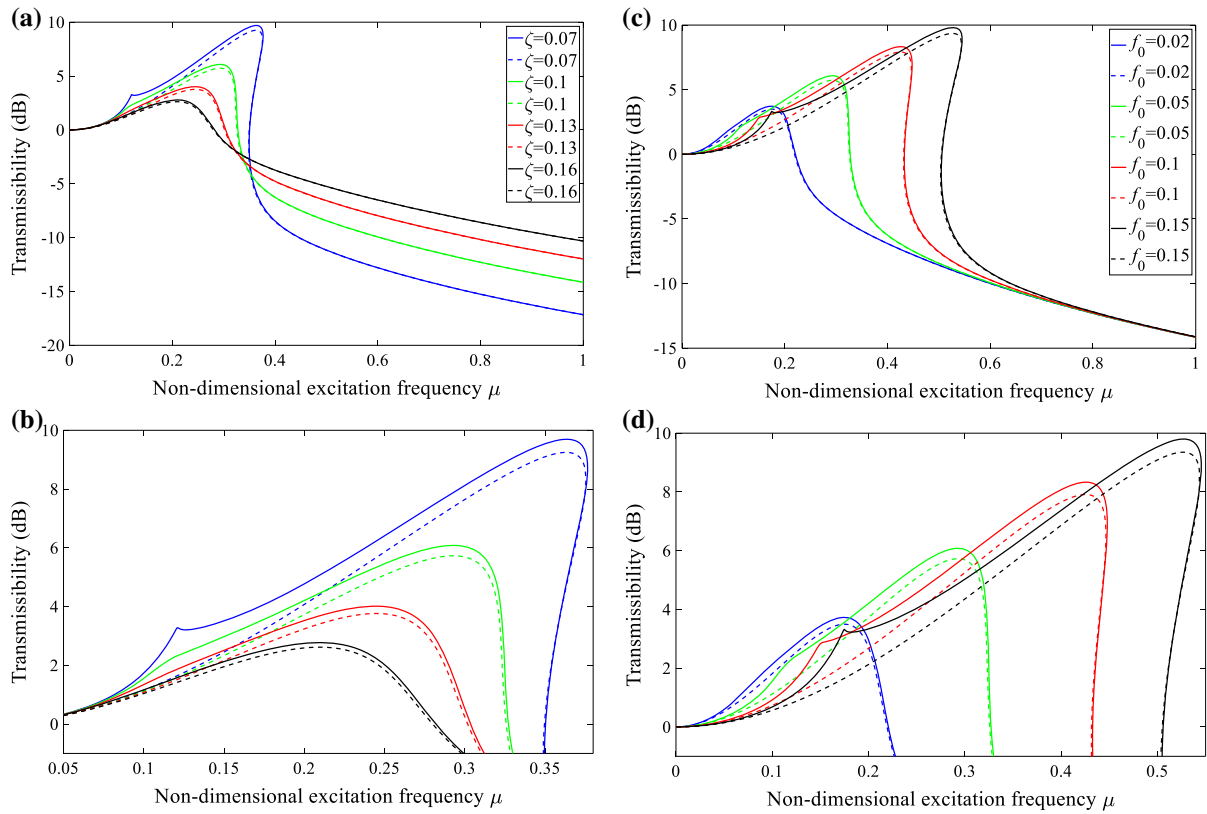


Fig. 20 Transmissibility versus non-dimensional excitation frequency **a** with different values of ζ when $\beta = 0.2$, $f_0 = 0.05$; **b** zoom of **a** in low-frequency range; **c** with different values of f_0 when $\beta = 0.2$, $\zeta = 0.1$; **d** zoom of **c** in low-frequency

range) (solid lines show the transmissibility curves when taking the superharmonic resonance into consideration; dashed lines show the transmissibility curves under the assumption of single-harmonic response)

the magnitude of influence. It is natural to think that the frequency range in which the superharmonic resonance has an effect corresponds to the “superharmonic region” mentioned in Sect. 4.3. This thought can be demonstrated by comparison of Figs. 19 and 20: On the one hand, further examination of Fig. 20 shows that the isolation frequency is almost unaffected by the superharmonic resonance, and the demarcation point that separates the frequency range where the effect of the superharmonic resonance perceptibly exists or not is near the isolation frequency (the transmissibility at frequencies lower than the isolation frequency is increased by the superharmonic resonance, while that at frequencies higher than the isolation frequency is hardly affected); on the other hand, comparison of Fig. 19 and 20 indicates that the superharmonic truncation frequency is approximately equal to the isolation frequency. Therefore, considering that the super-

harmonic truncation frequency is the right boundary of the “superharmonic region,” the frequency range in which the transmissibility is increased by the superharmonic resonance is just the “superharmonic region,” and it almost coincides with the frequency range lower than the isolation frequency. The effect of the superharmonic resonance is not only manifested in the increase in the transmissibility, but also in a slight change in the shape of the transmissibility curve: A small hump appears in the transmissibility curve of low-frequency range when considering the superharmonic resonance; the frequency at this hump corresponds to the frequency at the peak of the superharmonic energy factor curve; however, increasing ζ or decreasing f_0 will flatten this hump.

In order to quantify the magnitude of the influence of superharmonic resonance on the vibration isolation performance, we introduce the *transmissibility amplifi-*

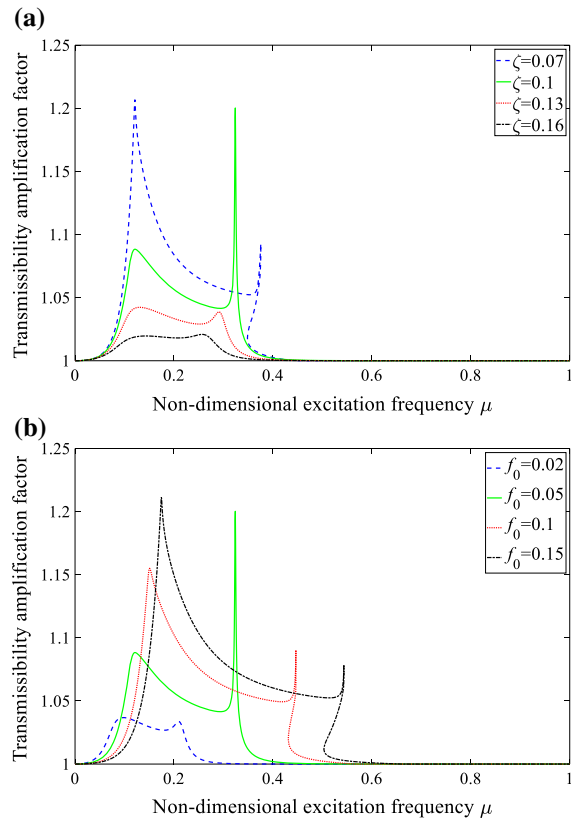


Fig. 21 Transmissibility amplification factor versus non-dimensional excitation frequency **a** with different values of ξ when $\beta = 0.2$, $f_0 = 0.05$; **b** with different values of f_0 when $\beta = 0.2$, $\xi = 0.1$)

cation factor (TAF), which is the ratio of the transmissibility calculated when considering the superharmonic resonance [using Eq. (53)] to the transmissibility calculated under the single-harmonic response assumption [using Eq. (54)]. Figure 21 depicts the TAF versus (non-dimensional) excitation frequency under different parameter conditions. The TAF has two peak values in the frequency domain. The frequency at which the TAF takes the first peak value corresponds to the frequency at the peak of the superharmonic energy factor curve, and larger peak value of the superharmonic energy factor leads to larger first peak value of the TAF. Further comparisons of Figs. 17, 18 and 21 suggest that the magnitude of the increase in the transmissibility is generally related to the superharmonic energy factor: The variation trend of the TAF with respect to the excitation frequency is basically similar to that of the superharmonic energy factor; larger superharmonic energy

factor leads to larger increase in the transmissibility. However, the frequency range close to the superharmonic truncation frequency seems to be an exception; in this frequency range, there appears the second peak in the TAF curve; the more serious the superharmonic resonance is, the closer the frequency of the second peak is to the superharmonic truncation frequency; if the jump phenomenon exists, the second peak occurs at the jump-down frequency (superharmonic truncation frequency), in which case the second peak becomes very sharp.

Although the vibration isolation performance of the QZS isolator is somewhat degraded by the superharmonic resonance, the QZS isolator is still a good passive vibration isolation approach. Here are three reasons. Firstly, the effect of the superharmonic resonance exists mainly in the “superharmonic region,” whereas the isolation performance at higher frequencies is almost unaffected. Secondly, the degree of degradation is not very large; the maximum TAF, for example, is only about 1.2 in Fig. 21. Thirdly, the isolation frequency almost remains unchanged when taking the superharmonic resonance into account, so there is still a wide frequency range with vibration isolation effect, which is much wider than the isolation region of an equivalent linear isolator.

6 Conclusions

The superharmonic resonance of the QZS vibration isolator is studied in this paper. After formulating the equation of motion, numerical simulations are conducted; it is shown that the QZS isolator will experience PH, SB, PD and SN bifurcations when varying system parameters, and various response types are generated under different parameter conditions, such as period- n ($n = 1, 2, 3, 4$) responses and chaotic response, among which the period-1 response can occur for a large region of parameter space. Further numerical analysis of the period-1 response shows that it contains not only primary harmonic but also multiple superharmonics, the frequencies of which are odd times the excitation frequency, and their amplitudes are relatively small compared to the primary harmonic. Based on the numerical findings, the superharmonic response is analytically calculated by using HBM, and the stability is analyzed by a semi-analytical method; it is shown that there is a narrow frequency range in which the superharmonic

amplitude decreases rapidly to nearly zero; if the excitation amplitude is larger than a certain value, three possible superharmonic solutions coexist in this frequency range, and the intermediate solution branch is unstable. In order to examine all of the superharmonics from a global perspective, two indices are proposed: The superharmonic energy factor characterizes the superharmonic energy proportion, and the superharmonic truncation frequency characterizes the excitation frequency range in which the superharmonic resonance perceptibly exists; it is shown that reducing nonlinear coefficient or excitation amplitude and increasing damping ratio are conducive to weakening the superharmonic resonance. To investigate the effect of superharmonic resonance on the vibration isolation performance, the force transmissibility is redefined which can take the superharmonics into account; it is shown that the superharmonic resonance degrades the isolation performance when the excitation frequency is lower than the superharmonic truncation frequency, and the degree of this degradation is closely related to the superharmonic energy factor; it is also shown that the frequency above which isolation occurs is almost unaffected by the superharmonic resonance, so the QZS isolator can still possess a much wider frequency range of isolation than the equivalent linear isolator.

Acknowledgements The authors would like to thank Prof. Zhao for the helpful suggestions on the results presented in this paper.

Compliance with ethical standards

Conflict of interest The authors declare that there is no conflict of interests regarding the publication of the paper.

References

- Shaw, A.D., Neild, S.A., Wagg, D.J.: Dynamic analysis of high static low dynamic stiffness vibration isolation mounts. *J. Sound Vib.* **332**, 1437–1455 (2013)
- Ibrahim, R.A.: Recent advances in nonlinear passive vibration isolators. *J. Sound Vib.* **314**, 371–452 (2008)
- Liu, C.R., Yu, K.P.: A high-static-low-dynamic-stiffness vibration isolator with the auxiliary system. *Nonlinear Dyn.* **94**, 1549–1567 (2018)
- Liu, C.R., Yu, K.P., Pang, S.W.: A novel eight-legged vibration isolation platform with dual-pyramid-shape struts. *Mechanica* **54**, 873–899 (2019)
- Fu, N., Meng, L.S., Wu, W.J., Sun, J.G., Su, W.H., Meng, G., Rao, Z.S.: Recent advances in quasi-zero-stiffness vibration isolation systems. *Appl. Mech. Mater.* **397–400**, 295–303 (2013)
- Carrella, A., Brennan, M.J., Waters, T.P.: Static analysis of a passive vibration isolator with quasi-zero-stiffness characteristic. *J. Sound Vib.* **301**, 678–689 (2007)
- Carrella, A., Brennan, M.J., Kovacic, I., Waters, T.P.: On the force transmissibility of a vibration isolator with quasi-zero stiffness. *J. Sound Vib.* **322**, 707–717 (2009)
- Carrella, A., Brennan, M.J., Waters, T.P.: Optimization of a quasi-zero-stiffness isolator. *J. Mech. Sci. Technol.* **21**, 946–949 (2007)
- Kovacic, I., Brennan, M.J., Waters, T.P.: A study of a nonlinear vibration isolator with a quasi-zero stiffness characteristic. *J. Sound Vib.* **315**, 700–711 (2008)
- Hao, Z.F., Cao, Q.J.: The isolation characteristics of an archetypal dynamical model with stable-quasi-zero-stiffness. *J. Sound Vib.* **340**, 61–79 (2015)
- Lan, C.C., Yang, S.A., Wu, Y.S.: Design and experiment of a compact quasi-zero-stiffness isolator capable of a wide range of loads. *J. Sound Vib.* **333**, 4843–4858 (2014)
- Huang, X.C., Liu, X.T., Sun, J.Y., Zhang, Z.Y., Hua, H.X.: Vibration isolation characteristics of a nonlinear isolator using Euler buckled beam as negative stiffness corrector: a theoretical and experimental study. *J. Sound Vib.* **333**, 1132–1148 (2014)
- Liu, X.T., Huang, X.C., Hua, H.X.: On the characteristics of a quasi-zero stiffness isolator using Euler buckled beam as negative stiffness corrector. *J. Sound Vib.* **332**, 3359–3376 (2013)
- Fulcher, B.A., Shahani, D.W., Haberman, M.R., Seepersad, C.C., Wilson, P.S.: Analytical and experimental investigation of buckled beams as negative stiffness elements for passive vibration and shock isolation systems. *J. Vib. Acoust.* **136**, 031009 (2014)
- Hu, D., Chen, L.Q.: Nonlinear vibration of a slightly curved beam with quasi-zero-stiffness isolators. *Nonlinear Dyn.* **95**, 2367–2382 (2018)
- Huang, X.C., Liu, X.T., Hua, H.X.: On the characteristics of an ultra-low frequency nonlinear isolator using sliding beam as negative stiffness. *J. Mech. Sci. Technol.* **28**, 813–822 (2014)
- Robertson, W.S., Kidner, M.R.F., Cazzolato, B.S., Zander, A.C.: Theoretical design parameters for a quasi-zero stiffness magnetic spring for vibration isolation. *J. Sound Vib.* **326**, 88–103 (2009)
- Xu, D.L., Yu, Q.P., Zhou, J.X., Bishop, S.R.: Theoretical and experimental analyses of a nonlinear magnetic vibration isolator with quasi-zero-stiffness characteristic. *J. Sound Vib.* **332**, 3377–3389 (2013)
- Wu, W.J., Chen, X.D., Shan, Y.H.: Analysis and experiment of a vibration isolator using a novel magnetic spring with negative stiffness. *J. Sound Vib.* **333**, 2958–2970 (2014)
- Li, Q., Zhu, Y., Xu, D.F., Hu, J.C., Min, W., Pang, L.C.: A negative stiffness vibration isolator using magnetic spring combined with rubber membrane. *J. Mech. Sci. Technol.* **27**, 813–824 (2013)
- Zheng, Y.S., Zhang, X.N., Luo, Y.J., Zhang, Y.H., Xie, S.L.: Analytical study of a quasi-zero stiffness coupling using a torsion magnetic spring with negative stiffness. *Mech. Syst. Signal Process.* **100**, 135–151 (2018)
- Zhu, T., Cazzolato, B., Robertson, W.S.P., Zander, A.: Vibration isolation using six degree-of-freedom quasi-zero stiffness magnetic levitation. *J. Sound Vib.* **358**, 48–73 (2015)

23. Kim, K.R., You, Y.H., Ahn, H.J.: Optimal design of a QZS isolator using flexures for a wide range of payload. *Int. J. Precis. Eng. Manuf.* **14**, 911–917 (2013)
24. Ahn, H.J., Lim, S.H., Park, C.K.: An integrated design of quasi-zero stiffness mechanism. *J. Mech. Sci. Technol.* **30**, 1071–1075 (2016)
25. Zhou, J.X., Xu, D.L., Bishop, S.: A torsion quasi-zero stiffness vibration isolator. *J. Sound Vib.* **338**, 121–133 (2015)
26. Wang, X.L., Zhou, J.X., Xu, D.L., Ouyang, H.J., Duan, Y.: Force transmissibility of a two-stage vibration isolation system with quasi-zero stiffness. *Nonlinear Dyn.* **87**, 633–646 (2017)
27. Wang, Y., Li, S.M., Neild, S.A., Jiang, J.Z.: Comparison of the dynamic performance of nonlinear one and two degree-of-freedom vibration isolators with quasi-zero stiffness. *Nonlinear Dyn.* **88**, 635–654 (2017)
28. Carrella, A., Brennan, M.J., Waters, T.P., Lopes Jr., V.: Force and displacement transmissibility of a nonlinear isolator with high-static-low-dynamic-stiffness. *Int. J. Mech. Sci.* **55**, 22–29 (2012)
29. Levinson, N.: Transformation theory of non-linear differential equations of the second order. *Ann. Math.* **45**, 723–737 (1944)

Publisher's Note Springer Nature remains neutral with regard to jurisdictional claims in published maps and institutional affiliations.